RULE-BASED MODEL SPECIFICATION WITH APPLICATIONS TO MOTONEURON DENDRITIC PROCESSING

A Thesis
Presented to
The Academic Faculty

by

Nicholas P. Shapiro

In Partial Fulfillment
of the Requirements for the Degree
Master of Science in Bioengineering in the
Wallace H. Coulter Department of Biomedical Engineering

Georgia Institute of Technology
August 2006

RULE-BASED MODEL SPECIFICATION WITH APPLICATIONS TO MOTONEURON DENDRITIC PROCESSING

Approved by:

Dr. Robert H. Lee, Advisor
Wallace H. Coulter Dept. of Biomedical Engineering
Georgia Institute of Technology

Dr. Robert Butera
School of Electrical and Computer Engineering
Georgia Institute of Technology

Dr. Astrid Prinz
School of Biology
Emory University

Date Approved: June 20th, 2006

ACKNOWLEDGEMENTS

No Grateful Dead quote here, although one might be in order. I send out a heartfelt thank you to all of those whom I have crossed paths with, for better or for worse. I would like to specifically thank my advisor, Bob Lee, for all the technical, philosophical, and moral guidance he aimed in my direction. Thank you, Bob, for taking a chance on this wayward biologist. I am forever indebted to all of my family and peers, be they of science, engineering, or otherwise. Randy Weinstein, for showing me what a BS from a liberal arts institution really means; Sarah Jones, for being the embodiment of diligence and commitment…a daily reminder of the core virtues of science; Chris Church, William Boatin and Edgar Brown, the three pillars of rigorous methodology; *all* past and present members of the Lee Group and the Neuro Lab with whom I have volleyed ideas with; Patrick DiCiccio, Brandon Denny, Thomas Namey and Ethan Winger, for years of witty repartee; my sister, Rachael, for the perspective; all four of my brothers, Jason, Travis, Daniel and Matthew, for their bull-headed confidence in me…Matt, you are the binder and my closest friend; my grandfather, Samuel, for the continual intellectual engagements, and my late grandmother, Evelyn, for her loving and caring that knew no bounds; all the Shapiros, Pabons, Balderstons, Veras, Stumps, Sacks, Katzs and Gamsers, for forming the best net a tight-rope walker could ask for; my parents, Raphael and Angelina, for their tough but undying love, Nilda and John, for their truly unconditional love; and, of course, the light of my life, Lauren, for being my cohort in criminally negligent humor, my lifetime companion in marriage and founding member of our *duprass*. Thank you all, so very much, for your generous contributions to my salt-moving strategies…*"What a long, strange trip it's been!"* –Jerry Garcia, 1970

TABLE OF CONTENTS

LIST OF TABLES

Page

LIST OF FIGURES

Page

SUMMARY

With the recent discoveries of phenomena such as plateau potentials, bistability, and synaptic amplification the focus of motoneuron research has been directed to the dendritic processes giving rise to these latent behaviors. The common consensus is that the mechanism behind bistability, an L-type calcium channel generating a persistent inward current (PIC), (Schwindt and Crill 1980; Hounsgaard and Kiehn 1985; 1989) is also responsible for the amplification of synaptic input in motoneurons. However, modeling studies utilizing only calcium-based PICs (Powers 1993; Booth et al. 1997; Elbasiouny et al. 2005; 2006) have been unable to reproduce the high degree of synaptic amplification observed in experimental preparations (Prather et al. 2001; Hultborn et al. 2003; Lee et al. 2003). The present work examines a theoretical amplification mechanism (electrotonic compression; Cook and Johnston 1997; 1999), based on a sodium PIC of dendritic origin, which acts to supplement the synaptic amplification due to the calcium PIC. Electrotonic compression is achieved by balancing the resistance and capacitance components of passive cable properties with proportions of inactivating and non-inactivating (i.e. persistent; NaP) sodium channels and delayed rectifier potassium channels (K_{DR}). The current goal is to test the "goodness-of-fit" between electrotonic compression and empirically established mechanisms.

The findings of this modeling study support the concept of a dendritic sodium PIC which acts to reduce the attenuation of synaptic currents enroute to the motoneuron soma. The working hypothesis is that the ratiometric expression pattern of NaP:K_{DR} giving rise to this mechanism takes the form of a distribution "rule" applied ubiquitously across the dendritic tree, while the plateau-producing L-type calcium channels are restricted to a more regionalized distribution pattern.

The modeling methodology utilized in this study is a moderate departure from the conventional, "data-driven", approach. Parameter estimation, when underspecified, was guided by a phenomenological, "top-down", perspective on motoneuron functionality. From this vantage point it was possible to "peer down" the hierarchy of processes extending from macroscopic behaviors to kinetic parameters and subsequently "pare down" the dimensionality of the (underspecified) parameter space. Beginning with an unbranched, equivalent cylinder representation, this study also demonstrates the power inherent to the controlled expansion of morphological complexity in an already complex model. The current trend of encoding model morphology from reconstructed histological templates only augments the inverse problem of specifying ion channel distribution. It is therefore imperative that the neural modeling discipline adopt more rigorous and/or less opaque methodologies, such as the one utilized here, to both accommodate and rein in this growing complexity.

INTRODUCTION

Recent studies demonstrating the variety of ion channels located in the dendrites of motoneurons suggest that active conductances play a major role in whole-cell input processing (Wolff et al. 1998; Carlin et al. 2000b; Li and Bennett 2003). Complex behaviors, such as firing rate acceleration and synaptic amplification, arising as consequences of active dendrites have been the topic of much experimental and theoretical research. Attention has been disproportionately focused on one such behavior, known to the motor control community as "bistability", which can be most succinctly defined as hysteretic (or, history-dependent) stable firing or quiescence evoked by the same input (Schwindt and Crill 1980; Bennett et al. 1998; Lee and Heckman 1998a). It is a commonly held belief that a single type of voltage-dependent ion channel underlies both the synaptic amplification and bistable phenomena.

Several complicating factors hinder the direct, experimental access to the dendrites of motoneurons. Spinal motoneuron somata are very large (40-60 μm; Donselaar et al. 1986) and while this makes them a relatively easy target for intracellular recordings it also has the unfortunate effect of making membrane potential difficult to control under voltage clamp. A further nuisance is the extensive arborization of the dendritic tree and expanse of dendritic projections (>10 levels of branching and processes reaching >2 mm from the soma; Cullheim et al. 1987b; a) which, again, makes for poor space clamping of the dendrites. The volume occupied by the dendritic tree also creates difficulties for *in vitro* studies with organotypic slices. Some promising results have been recently obtained with organotypic and primary culture preparations (Larkum et al. 1996; Kuo et al. 2005) however with the limitation that only early stages of development (i.e. embryonic E12-E14) can be studied. This leaves only costly *in vivo* preparations and

half-century old techniques as the sole avenue for mature motoneuron experimentation. This being the current state of things, a case can be made that motoneuron experimental research has hit a wall.

Over the past several decades theoretical approaches to describing motoneuron behavior have been successful in modeling discrete facets of a much larger picture, however there has yet to emerge a unified model of form and function. This is likely due to our underestimate of the complexity inherent to these neurons and to our inability to manage such complexity with paradigmatic rigor. The present state of motoneuron modeling can be divided into two main thrusts, 1) bottom-up complexity management of underspecified parameter spaces, resulting in combinatorial redundancies of model output, by the design and development of parametric search algorithms and, 2) top-down complexity management of realistic morphological geometries by the employment of sub-micrometer resolved histological reconstructions constraining the compartmental connectivity. While the entire field suffers from the limited resources afforded by general-purpose computing hardware (for advances in custom-computing see Graas et al. 2004; Weinstein and Lee 2006), each of these thrusts has its own subset of successes and failures. Automated parameter searches (Vanier and Bower 1999; Keren et al. 2005) and genetic algorithms (Taylor and Enoka 2004) are most effective at refining output metrics and perform rather poorly at finding emergent behaviors such as synaptic amplification (i.e. such searches converge upon parameter sets producing target behaviors known *a posteriori*). Incorporating highly detailed geometric constraints, based upon realistic morphology, into compartmental modeling studies fortifies the validity of conclusions derived from simulation data yet excess realism forsakes the principles of model reduction and hinders the throughput of batch simulations. The general dearth of structured methodology within the neuronal modeling discipline needs to be addressed, therefore the present study adopts a rule-based modeling framework with top-down (or teleological) hierarchy

that simultaneously makes hypotheses and assumptions explicit while bounding the vast parameter space giving rise to meaningful behavioral outputs.

Under the guidance of these organizing principles this study seeks to shepherd the empirical efforts of motoneuron research to greener pastures. In particular, this study examines the "goodness-of-fit" of observed and theoretical mechanisms of synaptic amplification in motoneurons, integrated in a quantitative model and cultivated by teleological considerations.

Physiological Background

Bistable firing states are a direct repercussion of incomplete channel inactivation/deactivation. The particular output state observed is contingent upon the immediate history of membrane potential trajectory, which is monitored and driven by nonlinear and embedded/coordinated (i.e. voltage- or concentration-dependent) conductance control. Transition between states is unidirectional such that stable firing cannot arise spontaneously but must have been previously evoked by synaptic or injected stimulus. This prerequisite excitation, be it of natural (synaptic input) or artificial (electrode driven) origin, generates a sustained depolarization of the dendritic tree known as the "plateau potential" which is the governing mechanism behind bistable firing patterns (Schwindt and Crill 1980; Hounsgaard and Kiehn 1985; Carlin et al. 2000a).

Experimentally, the formation of the plateau potential is observed to occur in a rapid, all-or-none fashion when elicited by synaptic activation and/or somatic current injection causing acceleration in action potential firing (Bennett et al. 1998; Lee and Heckman 1998b). This acceleration gives rise to a hysteresis in the current-dependent firing rate function (F-I relation) of the motoneuron (Lee and Heckman 1998a). Schwindt and Crill

showed that this voltage bias was due to the incomplete inactivation of an inwardly rectifying calcium conductance which activated with a low voltage threshold (i.e. close to the resting membrane potential, or RMP) and was of dendritic origin. The ion channel with these properties belongs to a class of α-subunit isoforms with highly conserved amino acid sequence homology collectively called, L-type calcium channels (Hille 1992). Ionic currents with these general attributes (i.e. regenerative currents with incomplete inactivation) are hereafter referred to as persistent inward currents (PICs) and much of this work is dedicated to examination of their functional roles in motoneuron input processing.

Known and Theoretical Modes of Amplification

An important discrepancy was noted by Powers and colleagues when they made an accounting of synaptic current arriving at the soma ("effective synaptic current", or I_N) versus the current required to elicit the discharge rates necessary to produce functional levels of muscle contraction force (Powers and Binder 1995). At high levels of synaptic activity the somatic currents were insufficient to give rise to even modest amounts of muscle contraction, and motor unit recruitment was projected to not exceed postural tone. Somehow there was a current deficit in the F-I budget and a potential solution to this inconsistency was found in a mechanism that was assumed to promote amplification of synaptic inputs. PICs enable long durations of self-sustained firing even in the absence of excitatory input (Lee and Heckman 2000; Heckman et al. 2003).

It was later discovered that the excitability of these currents was directly managed by descending control from the brainstem (e.g. reticulospinal tracts) of the motoneuron monoaminergic state (Hounsgaard and Kiehn 1985). Furthermore, upon applying ionotropic input via monosynaptic Ia excitatory afferent stimulation at various holding

potentials (both hyperpolarized and depolarized with respect to RMP; Lee and Heckman 2000) showed that Ia I_N exhibited a strong voltage-dependence (i.e. increases with depolarized holding potentials) ultimately reaching its peak amplitude in the neighborhood of spike threshold potentials and also demonstrated that although PICs do not invariably evoke bistable firing (in fact, only Type S motoneurons exhibit completely bistable firing), they still enhance excitatory synaptic inputs in motoneurons of various input conductances.

These discoveries helped to cultivate the contemporary belief that L-type calcium-based PICs are the sole mechanism responsible for amplifying synaptic inputs to spinal motoneurons. However, Li and colleagues showed that in addition to the L-type calcium current a sodium-based PIC, displaying activation properties consistent with a dendritic origin, made a substantial contribution to the PIC as seen from the soma in chronic spinalized rats (Li and Bennett 2003; Li et al. 2004; there has since been similar findings in acute spinalized rats, Bennett 2006, unpublished report). This sodium PIC was shown to be intimately linked to action potential initiation and rhythmic firing (Lee and Heckman 2001; Harvey et al. 2005); while these findings suggest that sodium PICs contribute to synaptic amplification the exact nature of this role remains uncertain.

Whole-Cell Transfer Function Gain (Known)

Signal amplification occurs when the magnitude of output exceeds the input to a system. The boosting current introduced with PIC activation results in a fundamental modification of the motoneuron input-output relationship, or transfer function (*H(s)*, where *s* indicates parameterization in the complex-frequency domain for voltage or current inputs and outputs, *X(s)* and *Y(s)*, respectively; see equation 1 below).

$$Y(s) = H(s) \cdot X(s) \text{ where } H(s) = \frac{zeros(s)}{poles(s)} \qquad (1)$$

Under current clamp conditions the whole-cell open-loop transfer function, *H(s)*, is very complex and, in fact, presently unknown. This is because at increasing levels of injected current the neuron transitions from linear time-invariant (LTI) to a nonlinear, hysteretic system. What is apparent from experimental time-series is that the formation of the plateau potential causes a firing state transition whereupon the F-I slope (i.e. the *gain* of discharge frequency per change in injected current) is multiplicatively enhanced.

The range of injected current over which the presence of a plateau potential produces an enhanced, and nearly linear, gain is termed the core region of the secondary F-I range (Kernell 1965a). Upon further current injection the plateau eventually saturates and additional current does not increase the firing rate; this is commonly referred to as the tertiary range of the F-I function. Following the onset of repetitive firing, but prior to the plateau potential onset, the rate of discharge settles into a nearly linear increasing function of injected current which is termed the core region of the primary range. F-I transition from primary to secondary ranges is often discontinuous (under current step analysis) or of sigmoidal shape (with slowly ramped current) due to PIC genesis. These core regions are the source for most measurements of F-I gain reported in the literature despite the transient nonlinearities at their periphery.

These features of the motoneuron transfer function may derive from important functional mechanisms or may represent artifactual manifestations due to the mode of experimental observation. The antidromic (i.e. backwards, or soma-to-dendrites direction) initiation of dendritic plateaus by current injection following somatic microelectrode impalement, an act which itself introduces an artificial leakage current of unknown quantity, must drive a relatively smaller electrical load to the threshold for plateau onset compared to the orthodromic (dendrites-to-soma) arrangement. In theory, this set of circumstances could

fallaciously support all-or-none plateau activation and veil the natural course of its evolution.

As testament to the existence of such theoretical, intermediate states in the plateau potential genesis, Hultborn and colleagues witnessed a gradual increase in motoneuron discharge frequencies when somatic injection of slowly depolarizing current ramps were superposed with synaptic input via the descending CSTs, Ia afferent inputs, or contralateral antagonist afferent inputs (i.e. crossed extensor reflex; see Hultborn et al. 2003). They interpreted these observations as synaptic excitation giving rise to localized depolarization enabling local PIC recruitment. Incremental PIC recruitment has the general effect of grading the net current arriving at the somatic recording site, thereby facilitating a variable amplification scheme that is intrinsic to the motoneuron. This stands in stark contrast to the variable amplification due to the descending control of the motoneuron monoaminergic state. In essence, the relationship amongst these two schemes could act to bridge the gap between global modulation (i.e. monoaminergic-based lowering of the plateau potential onset threshold on a cell-wide or motor pool-wide scale) and local (i.e. dendritic), voltage-dependent computations.

Dendritic Transfer Function Gain (Theoretical)

Local dendritic circuits are sequentially connected by an axial resistance. For voltage commands in the vicinity of RMP, neuronal responses closely match those of a passive RC circuit and can therefore be considered as LTI systems. Equation 2 gives the transfer function of the RC circuit where the circuit output has a gain equal to the magnitude of the $H(s)_{sub}$ evaluated at the input frequency of the voltage clamp command. The series arrangement makes the current equivalent throughout this circuit (see equation 3).

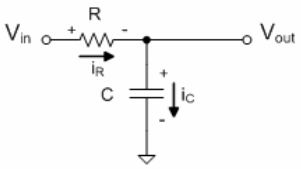

$$V_{out}(s) = V_{in}(s) \cdot \frac{1/Cs}{R + 1/Cs} \rightarrow H(s)_{sub} = \frac{1}{1 + \tau_m s} \qquad (2)$$

where $\tau_m = RC$;

$$I(s) = V_{in}(s) \cdot \frac{Cs}{1 + \tau_m s} \rightarrow \frac{I(s)}{V_{in}(s)} = H(s)_{sub} \cdot Cs \qquad (3)$$

Within a range of subthreshold potentials near RMP, intracellular electrode current produces a sustained depolarization which, when maintained under voltage clamp conditions, increases linearly. This subthreshold current-voltage (I-V) slope closely approximates the passive input conductance secondary to the distribution of steady-state leakage channels and the neuronal morphology. Assuming an ideal electrode with proportional gain, k, ($E(s) = H(s)_{\text{electrode}} = k, \forall s \in X(s)$), the subthreshold voltage commands, $X(s)_{sub}$, produce nearly linear current outputs, $Y(s)_{sub}$, due to a whole-cell transfer function, $H(s)_{sub}$; see equation 4, below. The closed-loop transfer function (equation 5) is essentially a high-pass filter:

$$Y(s)_{sub} = E(s) \cdot H(s)_{sub} \left(X(s)_{sub} - Y(s)_{sub} \right) \qquad (4)$$

$$\frac{Y(s)_{sub}}{X(s)_{sub}} = \frac{kH(s)_{sub}}{1 + kH(s)_{sub}}, \text{ where } E(s) = k \qquad (5)$$

The closed-loop transfer function, $H_{CL}(s)$, with proportional feedback gain, k, is given in equation 6. In the time domain the impulse response, $h_1(t)$, (equation 7) is a product of two exponentials scaled by the membrane time constant, τ_m. This response begins from

k/τ_m at $h_1(0)$ and asymptotically approaches zero. This approach is more rapid for small τ_m or large ω and can thereby be viewed as a low-pass filter.

$$\frac{Y(s)_{sub}}{X(s)_{sub}} = \left.\frac{k\left(\frac{\omega}{s+\omega}\right)}{1+k\left(\frac{\omega}{s+\omega}\right)}\right|_{\omega=\frac{1}{\tau_m}} = H_{CL}(s) \tag{6}$$

$$\left.\frac{Y(s)_{sub}}{X(s)_{sub}}\right|_{X(s)_{sub}=1} = \frac{k\omega}{s+(\omega+k\omega)} \Rightarrow h_1(t) = k\omega\left[\exp\left(-(\omega+k\omega)\cdot t\right)\right] \tag{7}$$

$$= \frac{k}{\tau_m}\cdot\exp\left(-t/\tau_m\right)\cdot\exp\left(-kt/\tau_m\right)$$

Evaluating the unit step response, $g_1(t)$, of this circuit shows that proportional feedback makes the system respond faster by improving the low-frequency response time, i.e., increasing k decreases (relative to time) the time constant for the step response; see equation 8. The counter-perspective on this situation is to say that *reducing the time constant is tantamount to increasing the gain*. Common to both viewpoints is the observation that increasing k effectively dilates the system time over the duration of the step response.

$$\left.\frac{Y(s)_{sub}}{X(s)_{sub}}\right|_{X(s)_{sub}=\frac{1}{s}} = \frac{k\omega}{s\left[s+(\omega+k\omega)\right]} \tag{8}$$

$$\Rightarrow g_1(t) = \frac{k}{k+1}\left[1-\exp\left(-(\omega+k\omega)\cdot t\right)\right] = \frac{k}{k+1}\left[1-\exp\left(-\frac{k+1}{\tau_m}\cdot t\right)\right]$$

In an ideal cable model (i.e. infinite length cable with no boundary conditions on voltage) under current clamp, the voltage trajectory during the rising phase of the subthreshold membrane response asymptotically approaches a steady-state voltage, V_{inf}, with a time course: $V(t) = V_{inf} - exp(-t/\tau_m)$. Transient subthreshold depolarizations return to RMP with an exponential decay scaled by the same time constant, τ_m, equivalent to the product of the membrane resistance and capacitance. A series resistance/capacitance arrangement extends throughout the cell so that in addition to local smoothing, subthreshold currents originating in electrically distant regions produce low-pass filtered voltage fluctuations that are attenuated to a degree proportional to physical distance from the recording site. This distance-dependent signal decrement is nonlinear and is analytically described in the ideal cable as:

$$\lambda = \sqrt{\frac{aR_m}{2R_a}} \tag{9}$$

$$L = \frac{l}{\lambda} \rightarrow 0 \text{ as}, R_m \rightarrow \infty \tag{10}$$

where the *space constant* (λ) is a function of the ratios of 1) membrane to axial resistance and 2) conductor volume to membrane surface area; thus the *resistivities* (i.e. cylindrical-*specific resistance*s), R_m and R_a, are oriented in the transmembrane (Ωcm^2) and axial (Ωcm) directions while a is the cable radius. The dimensionless representation of this spatial decrement (see equation 10), *electrotonic length* (L), is obtained by dividing the physical distance between source and sink, l, by λ.

If L can be minimized (as indicated in equation 10) then an oblique approach to amplification might be made (cf. Cook and Johnston 1997; 1999). To deal with the uncertainty inherent to physiological measures of L (Fleshman et al. 1988; Holmes and Rall 1992; Holmes et al. 1992), the model used in the present study was constructed with uniform R_m. Barring some kind of cytosolic microdialysis with a polar quantum liquid

that is superfluid at physiologic temperatures, R_a can also be faithfully regarded as constant on short time-scales and was likewise constrained in the model.

With *Y(s)* and *X(s)* as electrode current and holding potential, respectively, the transfer function is analogous to the I-V function when the capacitive component of *X(s)* is differentiated; as in equation 3. A zero slope conductance in the dendritic I-V function can be accomplished through RC (or, R_mC_m) compensation of the transient and steady-state components of the membrane response. Cancellation of passive cable properties requires a *scaling resistance/conductance* and a *negative capacitance*, each of appropriate temporal dynamics, to prevent the usual distance-dependent attenuation due to transmembrane current loss and capacitive changing. This sort of compensation would effectively "amplify" synaptic inputs, on a distance-dependent basis, while simultaneously invoking a high-fidelity transduction of synaptic currents to excitatory postsynaptic potentials (EPSPs) arriving at the soma. Therefore a linear step response for a single dendritic compartment (i.e. instantaneously reaches steady-state), in voltage or current, with a one-to-one scaling by input magnitude reveals the efficacy of this theoretical amplification mechanism.

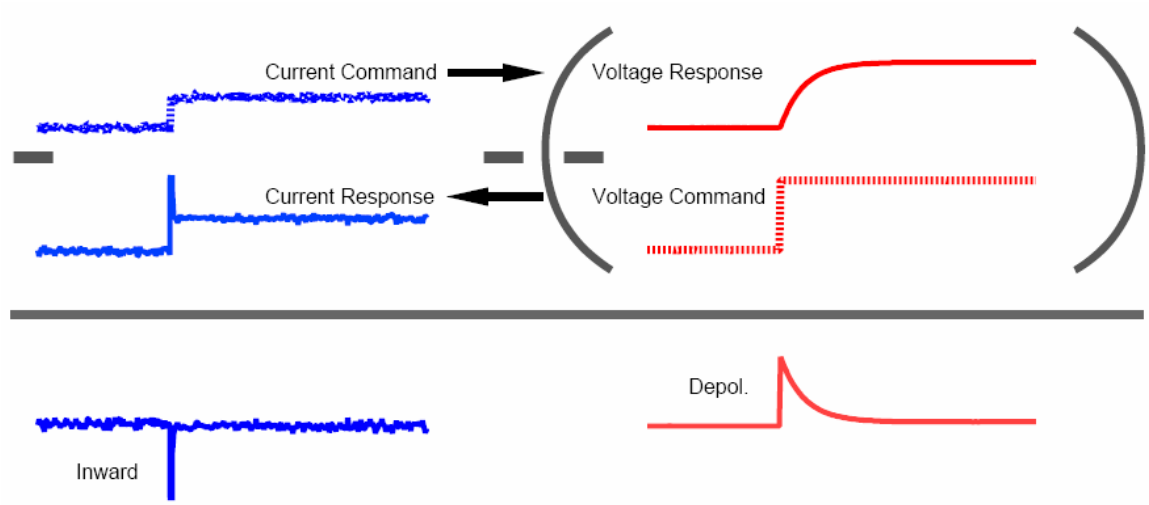

Figure 1.1 *Linearization of the membrane step response: Part 1.* Extracting the transient, capacitive

components of membrane responses. A current step command (100 pA) is low-pass filtered by a passive RC circuit "test-cell" to produce a familiar voltage response (50 mV, steady-state), and a voltage step command (50 mV) is similarly filtered to yield a current response (100 pA, steady-state). Subtracting each response from their corresponding command waveforms is analogous to high-pass filtering the command at a corner frequency equivalent to that of the membrane low-pass filter, leaving only the capacitive charging/discharging effects.

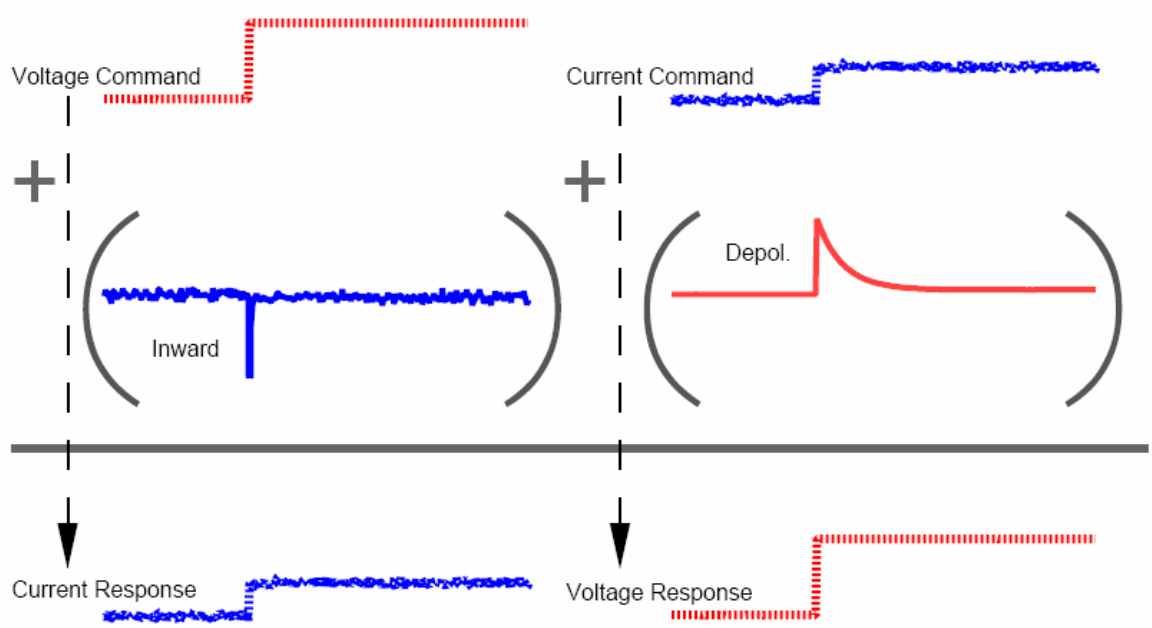

Figure 1.2 *Linearization of the membrane step response: Part 2.* Retrieval of high frequency components of the command waveform. Addition of the capacitive effects from Figure 1.1 (i.e. capacitive compensation of the passive circuit) amounts to a high-pass reciprocation of the passive membrane, effectively restoring the high frequency components to the step responses.

The membrane capacitance acts in opposition to synchrony between the voltage command and current response (i.e. the capacitance imposes a -90° phase lag in the feedback current). In order to facilitate a rapid membrane response, this phase lag must be reduced or eliminated with a fast current transient of inverse proportion as seen in bottom current trace of Figure 1.1. This phase shift requirement, a negative capacity compensation of the capacitive charging at the rising edge of an input, can be fulfilled with a rapidly activating and deactivating conductance; see Figure 1.1 and Figure 1.2.

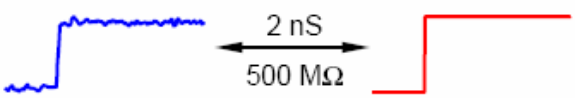

Figure 1.3 *Scaling the membrane response.* While the rising edge of the step is preserved by the capacitive compensation, the steady-state resistance (i.e. "leak" of 500 MΩ, or 2 nS) leads to a small disparity in the command-response magnitude. This steady-state current offset is compensated by scaling with the 2 nS persistent current; in a similar manner, the steady-state voltage offset compensation is achieved by scaling with a steady-state 500 MΩ resistance.

The scaling conductance has an implied directionality (inward) due to its role in canceling the steady-state leak conductance (outward) thus it is an energy source, or negative conductance, in terms of the sign convention used in electrophysiology. When a negative conductance is viewed as a constant inward current over a voltage range a PIC can provide a sustained negative conductance sufficient to cancel the passive leak conductance at steady-state, thereby remedying the magnitude disparity seen in Figure 1.2; see Figure 1.3. Therefore, all of the above criteria should be satisfactorily met with an appropriately sized population of persistent sodium channels (such as $Na_V1.6$ which has about a 2% ratio of non-inactivation to normal inactivation in a given channel population; Safronov et al. 1997).

Graded Gain Modulation

Computational capabilities are heightened when the number of states that a dynamic system can occupy is increased. The study conducted by Hultborn and colleagues (2003) demonstrated that dendritic PICs undergo a graded activation, leading to variable degrees of amplification, during dynamical states of somatic discharge activity. Meanwhile, a study by Prather and colleagues described a similar magnitude of amplification, and a linear summation of the two independent synaptic inputs they examined, yet did not detect a variable and increasing amplification with increasing rates of discharge (Prather et al. 2001). However, the latter experiments were tailored to examine changes in steady-state firing frequency while the former utilized procedures (e.g. somatic injection of

triangular current ramps during synaptic inputs) that focused on dynamic changes in motoneuron discharge rates. Yet, the linear summation seen in Prather *et al.* (2001) experiments was concluded by their demonstration that the firing effects induced by simultaneous activation of the two synaptic inputs was equivalent to the algebraic sum of the firing effects secondary to the activation of each input in isolation, which thereby suggests the existence of partially activated states in the dendritic PIC. Furthermore, Lee *et al.* (2003) described a large, graded increase in muscle stretch-evoked I_N at increasingly depolarized holding potentials, stating an average peak amplification factor about 2.7 times greater than the initial magnitude of amplification, yet reported that about half of the low input-conductance cells in the study displayed sudden surges in firing rate in response to muscle stretch (Lee et al. 2003).

These results imply a paradoxical situation in which dendritic PICs can undergo a smoothly graded activation meanwhile at least some portion of the PIC presents in a non-graded fashion. It is therefore a topic of interest as to what 1) types of intracellular mechanisms might be responsible for the gradation of PIC-dependent amplification and 2) degree of granularity might the gain modulus be expected to display during different modes of motoneuron activity.

SYNTHESIS OF THE MODEL

The motoneuron model is presented as a rule-based model that explains why and how specifications were made. Since this is a somewhat novel presentation format, the third and forth tiers (i.e. the traditional model specification) are at a conceptual level with the detailed mathematical description presented in the Appendix.

Formation of the model required the establishment of a hierarchical rule-set, which simultaneously constrains the model specification and explicates the assumptions/hypotheses of the model, followed by the actual implementation. In other words, the development proceeds from conceptualization to instantiation.

What is less evident is the iterative process that must take place in the likely event that the initial model instantiation is not successful. Although this refinement method is not part of the model generation proper, it is worthwhile to mention here the generalizable features of such procedures. Unsuccessful instantiations simply affirm an incomplete knowledge-base which, in turn, indulges otherwise unreasonable assumptions/hypotheses. The key remedy for this general case is the construction of a higher level rule(s) to ensure the specification of a parameter (or set of parameters).

Hierarchy of the Model Rule-Base (Conceptualization)

The rule-based model is constructed in four tiers. The top tier represents hypothesized *mechanisms* underlying behavioral specifications (which serve as validation; see Table 2.1). The second tier represents hypothesized *regulatory* actions for achieving those mechanisms. The third tier represents the *transporters* (i.e. ionic conductances, pumps

and buffers) and their mathematical description. This is the typical starting point for a traditional neuron model specification. Finally, the fourth tier represents the specification of all the *parameters* introduced in the third tier. These tiers, in their graphical and axiomatic forms, are presented below:

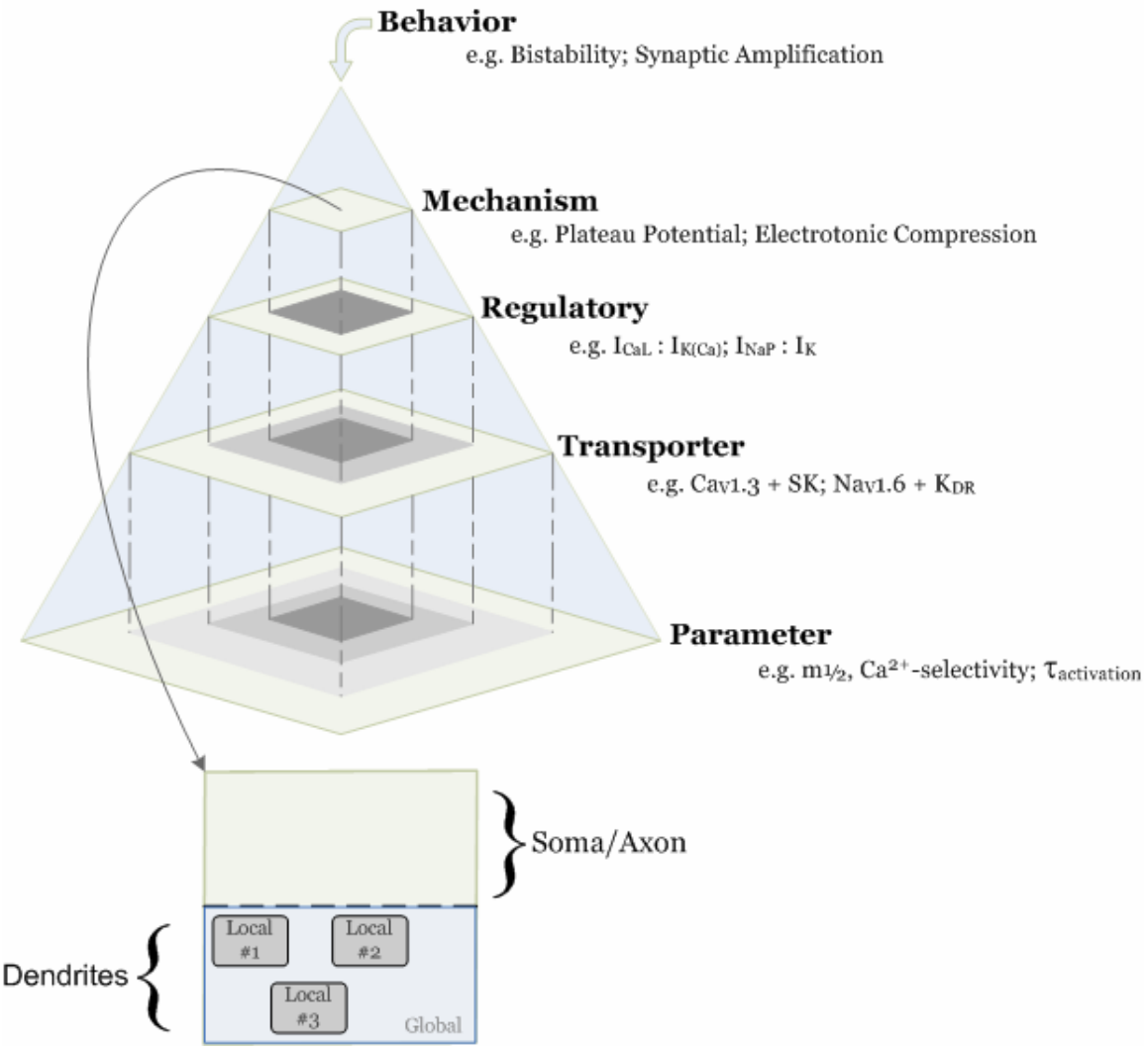

Figure 2.1 *Hierarchy of rule-based model tiers.* Four tiers, representative of the levels of neural functionality, are used as a teleological framework upon which model specification in the present study is based. Beginning with the validation of phenomenological behaviors, a top-down hierarchy of mechanistic components is established. Examples of these components are listed with each tier; semicolons separate experimentally validated from theoretical components of the experimental phenomena of bistable firing patterns and synaptic amplification, respectively. The spatial context in which the functional components operate is illustrated for the Mechanism Tier, but equally applies to all sub-tiers.

Mechanism Tier

Dendrites

1. Local zero electrotonic length over some voltage region (i.e. have a region of zero slope in the I-V relationship from steady-state up through higher frequencies).
2. Local, slowly-activating plateau potential capability (i.e. have a negative slope region in their I-V relationship near steady-state conditions).
3. Overall electrotonic length of 1.3 at hyperpolarized voltages (i.e. away from the effects of #1 above).
4. Proximal afterhyperpolarization (AHP) mechanism that is relatively insensitive to changes in action potential height.

Soma/Axon

5. A region of the neuron (presumably the axon hillock/ initial segment) where action potentials can be easily initiated. Initiation is presumed to require a local I-V relation that contains a negative slope region at moderate to high frequencies, but not necessarily at steady state. (Lee and Heckman 2001)
6. A somatic action potential generating (as opposed to initiating) mechanism.

Regulatory Tier

1. A local region of zero electrotonic length is achieved via fast sodium currents, with a small but notable persistent component, and potassium currents in the dendrites (achieving the zero electrotonic length is accomplished by establishing a ratio of sodium to potassium conductance membrane densities based on the characteristics of the conductances; e.g. changing the half activation voltage for potassium would change this ratio).
2. A local plateau generating mechanism is implemented via a slowly activating persistent calcium current (achieved with low threshold L-type calcium conductances in combination with SK type calcium-dependent potassium

conductances). As above, a ratio of calcium to potassium currents is established to produce a net negative slope region in the local I-V relation. It must be noted that this ratio assumes the above amplifying mechanism is in place (i.e. it builds upon that mechanism).

3. Dendrites are divided into 8 uniform compartments with a passive electrotonic length of 0.17 each.
4. We have chosen to overlap the AHP mechanism with the plateau mechanism. That is, the same L-type Ca^{2+} and SK channels responsible for the plateau are also responsible for the AHP. See Discussion for implications.
5. Action potential initiation is constructed from a combination of persistent and inactivating sodium conductances in a separate initial segment compartment. The compartment also contains delayed rectifier potassium (K_{DR}) conductances.
6. The bulk of the action potential amplitude as seen from the soma is generated by fast, inactivating sodium conductances (along with a corresponding amount of K_{DR} currents) present in a somatic compartment.

Transporter Tier

The sodium conductances used in this work inherently contain some persistence (Kuo and Bean 1994) and are conceptually distributed based on the level of persistence (Safronov et al. 1997). The K_{DR} conductance could be described as a "typical" (i.e. voltage-dependent, Boltzman-based conductances) version of such a current with the exception that it has been specifically tuned to adult cat lumbar motoneuron experimental data that exhibits non-constant time constants (Barrett et al. 1980).

Calcium currents are modeled as two different channel types, one with a relatively high activation and one with a relatively low activation (both isoforms are of the "L-type" calcium class). These two channels could also be described as "typical" voltage-dependent channels.

Ca^{2+}-dependent potassium conductances are always more difficult due to the intertwining issues of co-localization with calcium channels, and calcium buffering. The conductances modeled here are based on motoneuron experimental data (Barrett JN 1981), and more general calcium-dependent models (Sah 1993). Finally, h-currents are modeled after kinetic data from rat hypoglossal motoneurons (Bayliss et al. 1994) with exception that time constants have been dramatically reduced to fit spinal motoneuron behavior (Gustafsson and Pinter 1985). Detailed description of these channels will be presented in a subsequent section.

Parameter Tier

For the purposes of this work time constants, half-activation values, etc. are simply made consistent with the published behavior of the currents in motoneurons (See Discussion). In contrast, maximal conductance values (G_{Max}) were chosen to satisfy the Mechanisms tier and Regulatory tier specifications. The manner in which this was accomplished is described in the subsequent subsection.

TABLE 2.1 *OUTPUT METRICS FOR BEHAVIORAL VALIDATION*

				Ref
F-I Slope (Hz / nA)	1° Range	1.9 ± 1.0		1
at Steady State	2° Range	4.6		
Spike Threshold (mV)		14.2		2
		Partially Bistable	Fully Bistable	
Plateau Properties	Onset (mV)	-43.8 ± 3.7	-50.7 ± 4.5	3
	Offset (mV)	-47.3 ± 5.7	-60.0 ± 5.3	
	ΔV (mV)	3.5 ± 2.9	9.1 ± 2.2	
	I_{Onset} (nA)	11 ± 5.2	1.1 ± 3.6	
	I_{Offset} (nA)	9.0 ± 6.3	-4.5 ± 4.2	
	ΔI (nA)	2.1 ± 2.7	5.6 ± 2.1	
	I_{peak} (nA)	4.8 ± 6.4	-9.0 ± 3.8	
Dendritic I-V	Must include:	Zero slope conductance Negative capacitance SS leak compensation		4
Fast I-V **(I_{Fast} Onset Voltage)**	Significant correlation with:	Spike threshold F-I Gain		5
AHP Magnitude (mV)	Slow	4.9 ± 0.6		6
	Fast Fatigable	3.0 ± 0.2		
AHP Duration (ms)		77 ± 22		1
Input Conductance (μS)	Slow	0.63 ± 0.04		6
	Fast Fatigable	1.67 ± 0.0		
Spike Height (mV)		71 ± 14		1

References

1 Kernell, 1965a
2 Richter, et al., 1974
3 Lee and Heckman, 1998
4 Cook and Johnston, 1999
5 Lee and Heckman, 2001
6 Zengel et al., 1985

Model Generation (Instantiation)

Rather than starting with a spiking soma model then appending a passive structure to represent pentobarbital-anesthetized dendritic behavior and then adding plateau-generating currents as is typically done, the present model generation began with the dendrites of the decerebrate preparation where all of the active dendritic processing is observed. The central hypothesis here is that sodium channels in the dendrites generate a persistent sodium current that is just sufficient to cancel the leak conductance, resulting in

a voltage region of net zero conductance thereby reducing the steady state electrotonic length (i.e. Regulatory tier rule #1; cf. Figures 1.1 and 1.2). This provides the maximum possible amplification without creating a negative region that would be a potential site for rhythmic firing initiation in the dendrites (Lee and Heckman 1998a).

To fully comply with the concept of reducing electrotonic length, it is also necessary to consider the need for a negative capacitance. As mentioned above, the inactivating portion of the same dendritic sodium channels can fulfill that role. However, since a perfectly balanced RC compensation of the dendritic circuit would result in an infinite τ_m (i.e. as $R_m \rightarrow \infty$, the discharging of dendritic capacitance is increasingly shunted through the soma), inclusion of a K_{DR} conductance prevents an infinite τ_m as the membrane slope-conductance remains zero. Utilizing a ratio of $Na_V1.6$**:**K_{DR} appears to generate the best steady-state I-V behavior. This I-V relationship is established for a single dendritic compartment (normalized to a leak conductance of 1) as illustrated in Figure 2.2. The compartment is then replicated 8 times and these subunits are subsequently linked in series with axial resistances appropriately representative of L in a "typical" cat lumbar motoneuron dendrite (Regulatory tier rule #3). To this dendrite, passive soma and initial segment compartments are added. (The passive specifications of the initial segment compartment partially satisfy Regulatory tier rule #5).

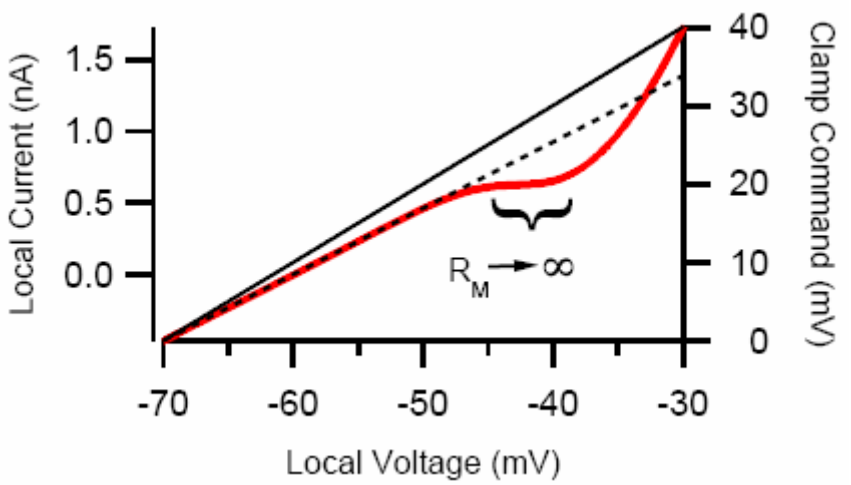

Figure 2.2 *Single dendritic compartment (local) I-V function.* The current response (bold trace) evoked by a slowly rising voltage command (thin trace) exhibits a reduced slope region in the presence of a ~ 3:5 ratio of K_{DR} to $Na_V1.6$, and ~1:1 ratio of I_{NaP} to I_{Leak} at steady-state. The stippled line denotes the input conductance (G_{IN} = 46 nS) measured near resting potential.

Active conductances in the initial segment and soma were subsequently specified. First, the initial segment is populated with sodium channels exhibiting approximately 2% persistence (Safronov et al. 1997); and Regulatory tier rule #5). It is worth noting that this produces an "A" spike that is consistent with that seen by Schwindt and Crill (1980). Next sodium channels with less persistence (Safronov et al. 1997) were added to the soma to generate a spike height of about 80 mV; K_{DR} is added to narrow the spike (Regulatory tier rule #6; values based on experimental data consistent with Kernell 1965a).

Calcium and SK channels were then added to generate the AHP as well as plateau potentials (Regulatory tier rules #2 and #4). However, the placement and make-up of these channels is still open to a great deal of uncertainty. Additionally, there are issues of Ca^{2+} pumping and buffering that are equally open to discussion. Consequently, while we have accomplished these tasks, it should be noted that the chosen distributions represent only one possible scenario rather than *the* solution to distributing these active mechanisms; Table 2.2 portrays this distribution. We have chosen to rely on only L-type

calcium and SK with no LVA calcium and with sufficient Ca^{2+} pumping to control Ca^{2+} concentration. The distribution is uniform throughout the dendrites with the exception of a substantial load of SK in the most proximal dendritic compartment. This increased load effectively produces the AHP as well as a large outward current that is known to appear experimentally just above threshold during voltage-clamped voltage ramps of the soma (Lee and Heckman 1998b).

TABLE 2.2 *DISTRIBUTION OF ION TRANSPORTERS*

Channel Type & G_{Max} (μS)	*Model Compartments*									
	Soma & Axon		*(proximal)*			***Dendrite***				*(distal)*
	IS	*Soma*	*1*	*2*	*3*	*4*	*5*	*6*	*7*	*8*
$Ca_V1.2$			0.86							
$Ca_V1.3$			0.03 (x8)							
h			0.2 (x8)							
SK			1	0.15 (x7)						
K_{DR}	1	4	0.905 (x8)							
$Na_V1.2$		6								
$Na_V1.6$	5		1.53							
Pumps & I_{Max} (nA)	***Soma & Axon***		*(proximal)*			***Dendrite***				*(distal)*
	IS	*Soma*	*1*	*2*	*3*	*4*	*5*	*6*	*7*	*8*
CaATPase			1.5 (x8)							
NCX			14.5 (x8)							

INITIAL ASSESSMENT AND VALIDATION

Basic Behaviors

Figures 3.1 and 3.2 illustrate the basic behavior of the model to standard protocols. The characteristics of singly elicited motoneuron action potentials (Figure 3.1), such as spike height and threshold (84.9 mV and 13.7 mV, respectively; see Richter et al. 1974) were reproduced sufficiently, as were AHP magnitude (3.95 mV) and duration (129 ms; defined as 95% recovery from maximum hyperpolarization; Kernell 1965a; Zengel et al. 1985). Standard current-voltage (I-V) and frequency-current (F-I) properties were within normal bounds (See Lee and Heckman 1998a,b for comparison to experimental data). F-I properties were assessed from firing evoked by a slow, 3 nA/s, current ramp of 15 nA peak amplitude (Figure 3.2A). The F-I gain (i.e. slope of the best linear fit to equivalent current ranges per firing range) is 2.53 Hz/nA and 6.67 Hz/nA in the primary and secondary ranges, respectively (Figure 3.2B). The current resulting from a slow (8 mV/s) voltage ramp (Figure 3.2C) is parameterized by membrane potential to produce the familiar I-V function (Fig. 3.2D). Arrows denote the ascending and descending phases of the I-V and F-I functions, and key features of the I-V function are projected to the ordinate and abscissa. The first point of zero slope on the rising phase (at -52.8 mV and 3.24 nA) corresponds to the plateau onset while the offset of this persistent inward current (PIC) occurs at -58.4 mV and 1.26 nA, a more hyperpolarized potential than the onset value (ΔV = 5.6 mV; defined as the magnitude of I-V hysteresis; cf. Lee and Heckman 1998a).

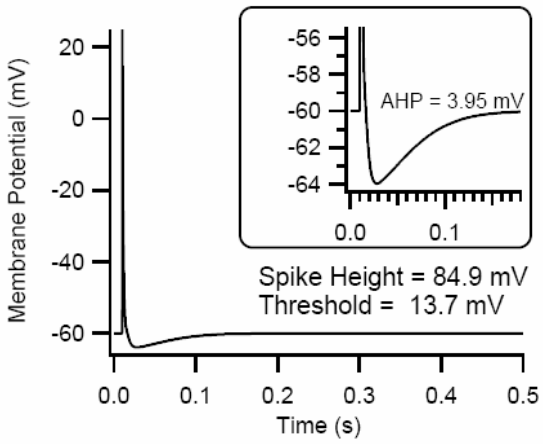

Figure 3.1 *Singly elicited action potential*. Spike evoked from a 30 nA current pulse of 5 ms duration. Gross morphology of the spike; spike height is 84.9 mV with threshold 13.7 mV above rest. *Inset*: A closer view of the AHP. Magnitude is 3.95 mV and duration is 129 ms (defined as 95% recovery from maximum hyperpolarization).

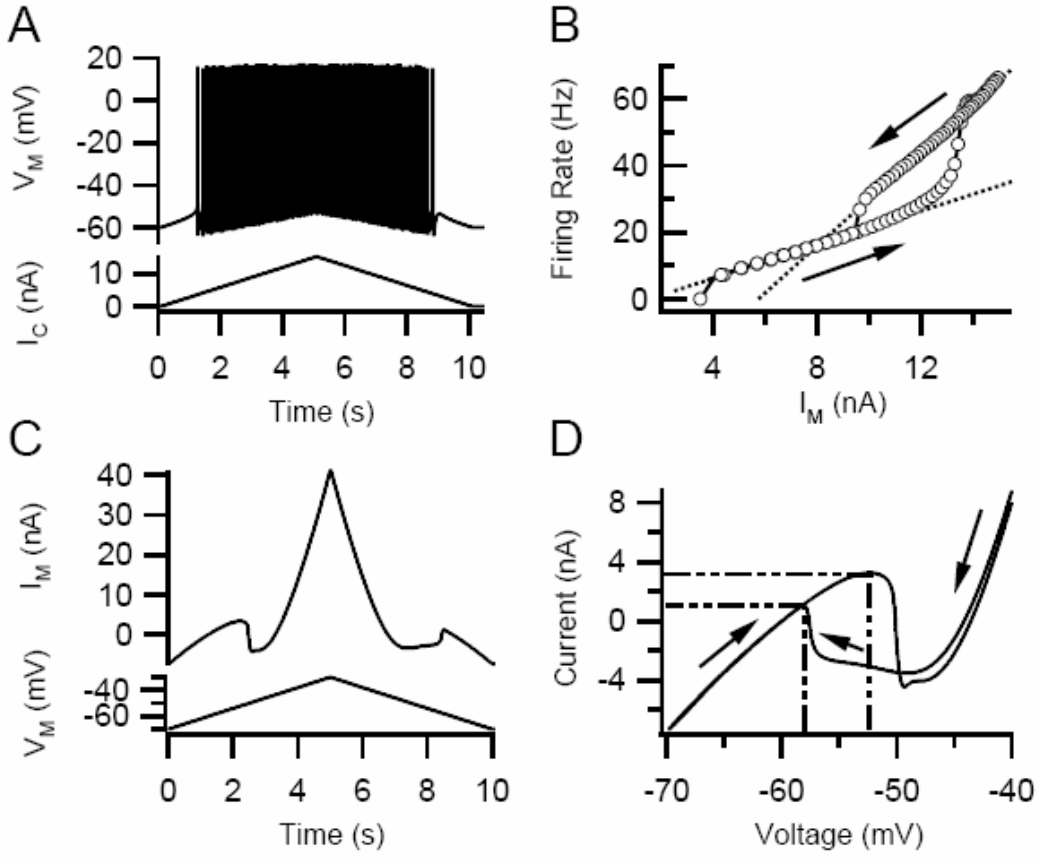

Figure 3.2 "*Base" model behavior under current and voltage clamp conditions. Panel A*: Firing in response to a slow current clamp ramp (3 nA/s). Here, and thereafter, membrane voltage-clamp and

current-clamp commands are denoted by subscript "C" while responses are indicated by a subscript "M". *Panel B*: F-I relation from *panel A*, with arrows indicating ascending and descending phases of the current command, illustrating the transition from primary (slope: 2.53 Hz/nA) to secondary range (slope: 6.67 Hz/nA). *Panel C*: Slow voltage clamp ramp (8 mV/s) and current record. *Panel D*: I-V parameterization from *panel C* with focus upon the hysteresis attributable to a slow decay of persistent inward current. Plateau onset and offset voltage and current values are indicated with broken lines (-52.8 mV, -58.4 mV, 3.24 nA, and 1.26 nA).

As an interesting aside, one possible repercussion of excitable dendrites is their potential ability to back-propagate action potentials originating at the soma or initial segment. Examination of the dendritic compartments for an elicited spike reveals that some degree of back-propagation does occur (Figure 3.3).

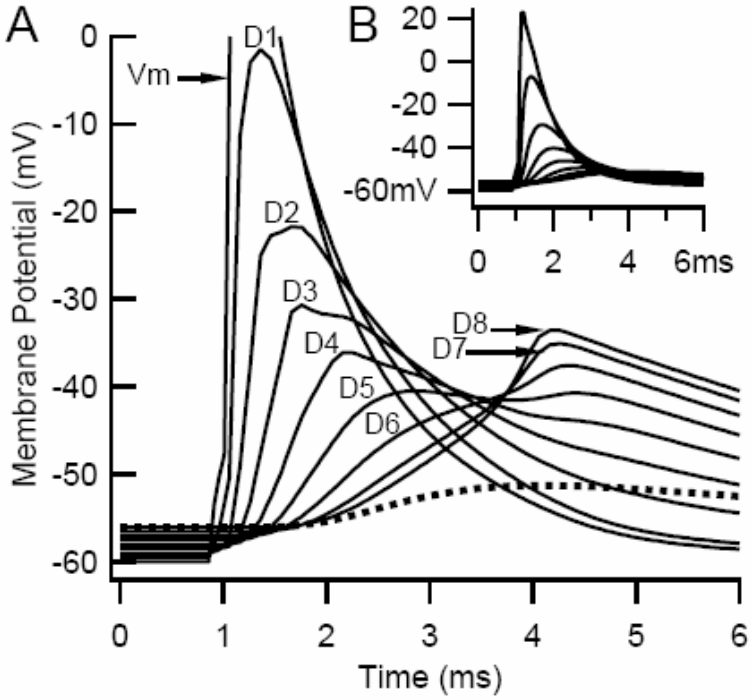

Figure 3.3 *Action potential back-propagation as a consequence of active dendrites.* Back-propagation of a somatically elicited action potential into the dendritic tree, with (main plot) and without (inset and dotted line representing D8 in main plot) dendritic voltage-gated sodium channels. Approximately 2.8 ms post stimulus, an isopotential state appears in the distal half of the dendritic tree (compartments D5 – D8). This state drops off rapidly with increasing proximity to the soma indicating the substantial electrotonic influence of the soma on the dendritic tree.

While these features fall within or closely to the range of experimentally observed values given in Table 2.1, they are not completely satisfying. For example, the steepness of the negative slope regions in the I-V curve is rather severe, and the current thresholds of hysteresis in the F-I relationship doe not coincide with those in the I-V relationship (I-V hysteresis encircles zero nA while the F-I hysteresis encircles a region nearly 10 nA higher).

Bistability and Dendritic Plateau Potentials

One key parameter whose value is not fully specified by the set of rules is the half-activation of the L-type calcium channels responsible for the dendritic plateaus. The baseline value of -41 mV was chosen to match experimental values (unpublished observation Bennett 2005). However, it is plausible that this half activation voltage might resolve the above hysteresis discrepancy (and thus, generate another hypothesis/rule). Consequently, we investigated the effect of altering the $Ca_V1.3$ half activation voltage (Figure 3.4).

Variation of the half-activation voltage value of the $Ca_V1.3$ altered the I-V hysteresis magnitude (as measured in voltage). Altering this value results in an unequal shift of onset and offset values for the plateau potential such that ΔV narrows from 9 mV to 6 mV to 3 mV for half-activation values -47 mV (hereafter referred to as the $Ca_V1.3^{-47}$ model), -41 mV ("base" model), and -38 mV, respectively. Significant transitions accompanying the narrowing are 1) the slope change of inward current upon descent of the voltage command (leftward arrows in Figure 3.4), 2) the increase in voltage range from rest to onset, and 3) the polarity reversal of offset current. These alterations are indicative of a fundamental change in the input-output relationship and represent a shift in the processing of excitatory synaptic inputs.

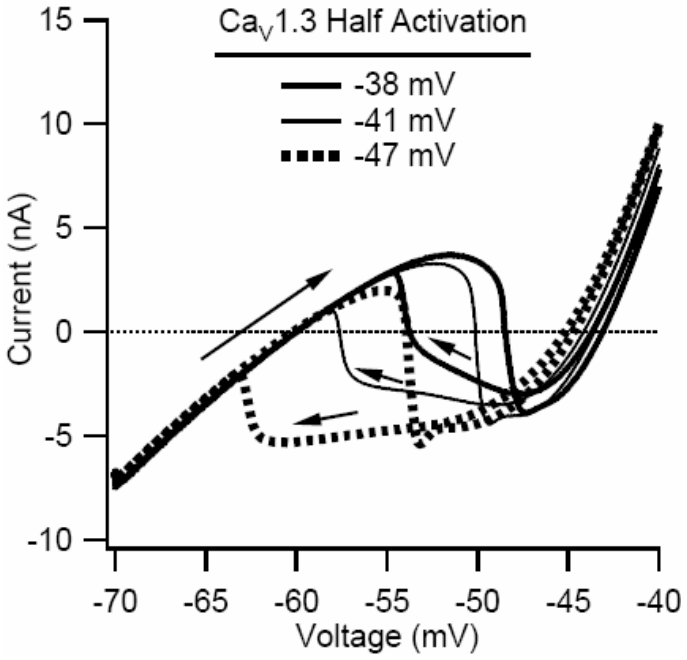

Figure 3.4 *$Ca_V1.3$ half-activation voltage and compression of I-V hysteresis*. Hysteresis is diminished both in current and voltage as $Ca_V1.3$ half-activation is depolarized. Note that the -47 mV case is the only one that would clearly result in firing bistability about zero input.

Hyperpolarizing the half activation voltage resolved the hysteresis discrepancy between F-I and I-V relationships (Figure 3.5). The $Ca_V1.3^{-47}$ model was capable of bistability about zero input in that the model could be transitioned from quiescence to sustained, rhythmic firing with a brief, uniformly distributed, excitatory synaptic input which was subsequently withdrawn (Figure 3.5A). This was only possible with sustained input in the base model (i.e. the bistability was not about zero input). Additionally, the discrepancy between the F-I hysteresis and the I-V hysteresis was notably reduced (Figure 3.5B) and F-I gain in the primary region of the $Ca_V1.3^{-47}$ model was essentially equivalent to the base model at 2.61 Hz/nA. The secondary regions of both F-I functions, also well aligned, were fitted with two lines (not shown) due to the degree of curvature within this range. Within the core region of the secondary range (defined as the range

over which a straight line intersects the largest number of points) the gain was 6.67 Hz/nA for both the "base" and $Ca_V1.3^{-47}$ models.

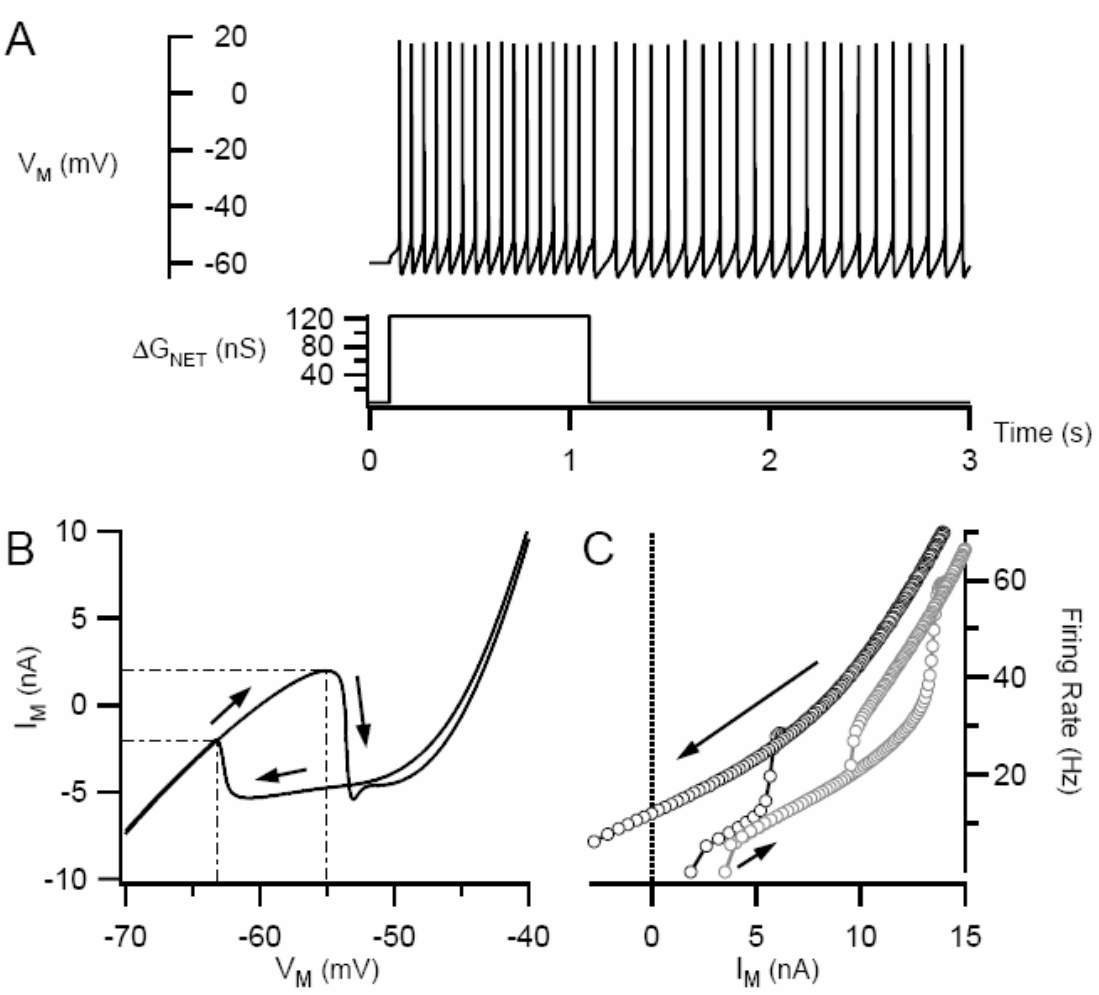

Figure 3.5 *Genesis of bistable firing. Panel A*: Fully bistable response of the $Ca_V1.3^{-47}$ model version to the classical method of modeling Ia synaptic input (i.e. 7.7 nS step conductance change in all dendritic compartments, persisting for one second). *Panel B*: The I-V function of the $Ca_V1.3^{-47}$ model has plateau onset and offset voltage and current values of -55.2 mV, -63.7 mV, 1.96 nA, and -2.20 nA. Comparison with Figure 2D shows a downward and leftward translation due to the synaptic facilitation of plateau formation. *Panel C*: The F-I function for the $Ca_V1.3^{-47}$ model; note the bistablilty about zero current. The primary range gain is 2.61 Hz/nA. The secondary range gain for both model versions is essentially the same, 6.67 Hz/nA.

Thus, it would seem that simply altering the $Ca_V1.3$ half activation voltage results in a better model. However, we have yet to consider synaptic amplification.

Synaptic Amplification and Electrotonic Compression

To assess synaptic amplification a mock excitatory Ia synaptic input was applied uniformly to the dendrite to approximate that used experimentally (Figure 3.6A; Lee and Heckman 2000). The input consisted of a steady component (2.75 nS, 22 nS net) and a dynamic component, which was exaggerated for better illustration (pulse train magnitude of 16.5 nS, 132 nS net). While this input elicits a plateau, there is no apparent amplification of the transient pulses as expected (Figure 3.6B). The model is capable of amplification, but only if the plateau is blocked (by setting $Ca_V1.3$ conductance to zero; Figure 3.6D). It would seem that plateaus and electrotonic compression-based amplification are not compatible despite being due to separate mechanisms. The problem is that the plateau pushes the distal dendrites above the voltage range of the electrotonic compression. Efforts to rectify this by altering the positioning and/or magnitude of the plateau were not successful (e.g. $Ca_V1.3^{-47}$; Figure 3.6C).

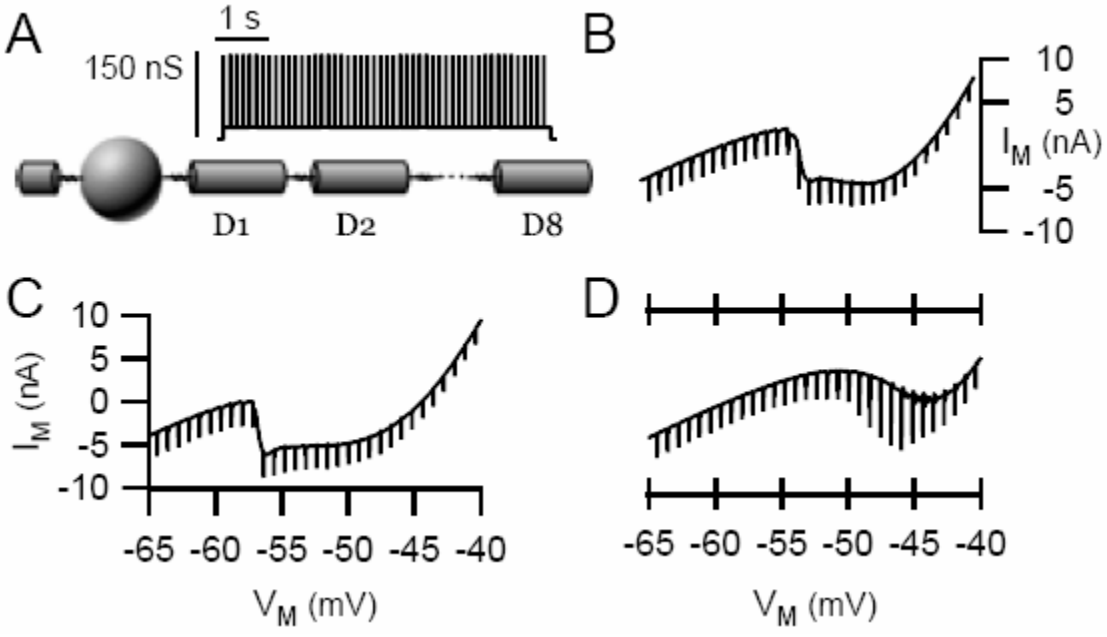

Figure 3.6 *Electrotonic compression versus plateau potential formation. Panel A*: macroscopic properties of the composite (i.e. mixed high and low frequency) synaptic input and the dendritic compartments to which it is applied. A 10 Hz pulse train (offset by a 2.75 nS step of long duration) of 16.5 nS, 3ms duration pulses serves as the waveform driving the synaptic conductance injection in each

dendritic compartment. Both "base" model simulation (*panel B*) and $Ca_V1.3^{-47}$ model simulation (*panel C*) display no significant amplification of EPSCs during the plateau. Note that the base simulation shows a small quantitative level of amplification just prior to plateau onset, which is not readily apparent (amplification factor = 1.09). *Panel D*: Blocking plateau reveals amplification. The amplification of EPSCs following the zero slope point is approximately twofold (amplification factor = 2.11) when $Ca_V1.3$ is removed. This indicates that plateaus and amplification may not be compatible in the same dendrite.

Amplification via electrotonic compression and plateaus can be made compatible if they are isolated from one another. Thus a new high-level rule/hypothesis is needed to constrain the model: "Slow, Ca^{2+}-based, plateau capability must be specified with regard to dendritic region."

The act of splitting the dendritic tree suggests that the addressing of rules to specific anatomical sites (i.e. dendrites, and soma/axon) requires more spatial resolution. We therefore subdivided the dendritic site into three, discrete regions: 1) the Ca^{2+}-plateau zone (D2A-D8A) for amplification of low frequency synaptic inputs, 2) the Ca^{2+}-plateau-free zone (D2B-D8B) for high frequency amplification and, 3) the proximal zone (D1) where AHP regulation and amplification-scheme integration occurs. These changes are implemented in the Mechanism tier where the anatomical origins of functional properties are now categorized per dendritic region as rules that are applied either regionally (e.g. localization of the Ca^{2+}-plateau in the "A" branch) or ubiquitously (e.g. local zero electrotonic length). While the rules themselves remain unaltered, the Mechanism tier is now resolved as depicted in Table 3.1.

TABLE 3.1 *ENHANCED SPATIAL RESOLUTION OF MECHANISM TIER RULES*

Rule #	Dendritic Zone for Rule Application		
	D1	**D2A-D8A**	**D2B-D8B**
1	■	■	■
2	■	■	
3	■	■	■
4	■		

Thus a "split-dendrite" model version was created by cutting the dendrite in half down to D1 (i.e. all conductances were divided equally between the two halves; Figure 3.7A). The $Ca_V1.3$ conductance was subsequently removed from the "B" branch thereby eliminating plateaus from that branch. Since the model now effectively had only half the plateau generating current, the $Ca_V1.3$ G_{Max} and maximal Ca^{2+}ATPase pumping rate were doubled while SK G_{Max} was halved (within the "A" branch) to meet the requirements of the regulatory rule governing plateau formation. This model version, which has an additional rule/hypothesis governing regional plateau distribution, exhibits a synaptic amplification factor of 1.9 (Figure 3.7B) and bistability (Figure 3.7C). Furthermore the F-I hysteresis (Figure 3.7D) coincides with the I-V hysteresis (i.e. both encircle zero input).

The dendritic voltage profiles during the synaptic protocol pictured in Figure 3.7B reveals the effectiveness of the branchwise separation of the two dendritic amplification mechanisms implemented in this model (see Figure 3.8). The electrical decoupling, which is markedly enhanced by the proximal (D1) load of SK conductance, increases with distance from the soma with a maximum difference of 12 mV between branches. Complete formation of the Ca^{2+}-plateau is achieved in the dendritic compartments of branch A verifying that the presence of the pre-established $Na_V1.6$ and K_{DR} ratio giving rise to electrotonic compression in no way impedes the plateau potential.

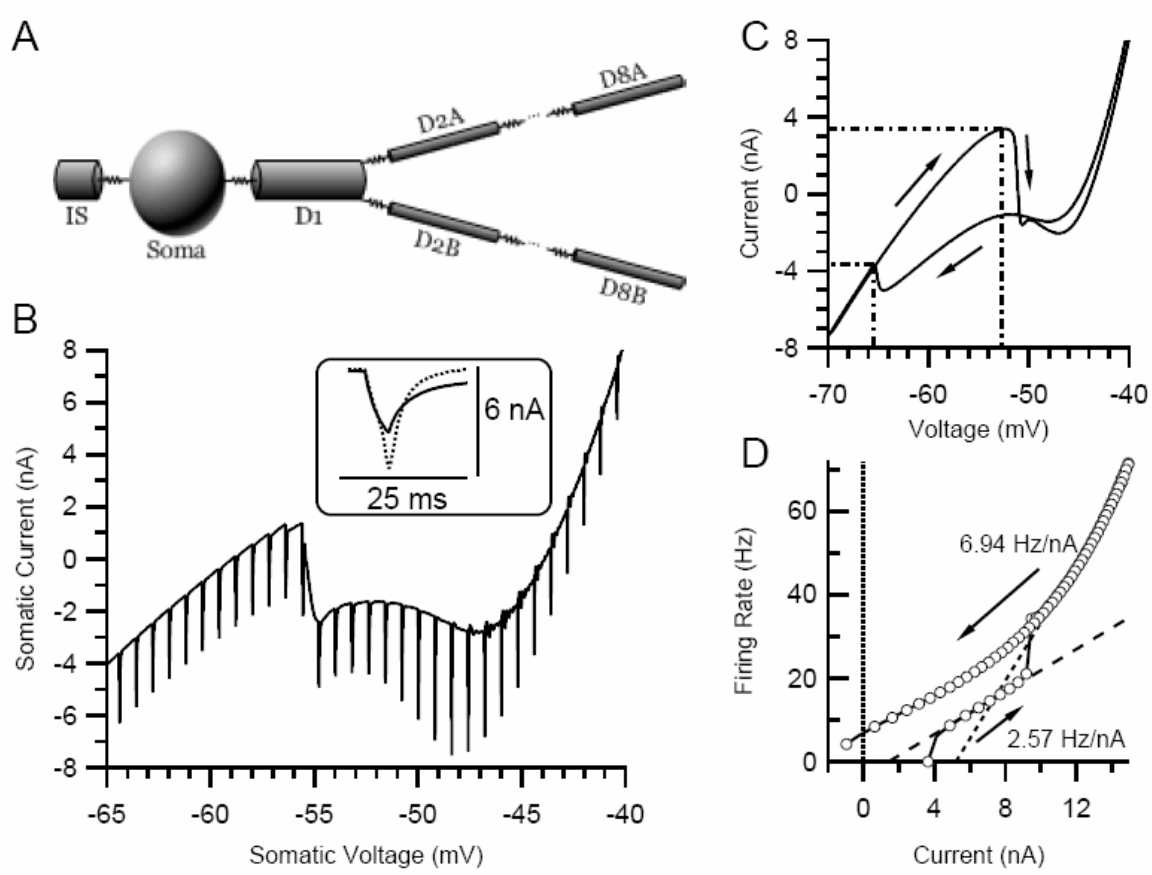

Figure 3.7 *Characterization of "split-dendrite" model version. Panel A*: "split-dendrite" illustration. Darkened compartments indicate those receiving synaptic input during a uniform input protocol. *Panel B*: The somatic I-V function with I_N resulting from uniformly distributed synaptic input on the dendritic compartments in one branch of the "split-dendrite" model. The branch receiving synaptic input (denoted branch B; compartments D2B-D8B, as illustrated in *panel A*) lacks the $Ca_V1.3$ conductance, but is otherwise identical to the other secondary dendrite. Synaptic input, per compartment, is a 10 Hz pulse train composed of 16.5 nS conductance changes of 3ms duration each, offset by a 2.75 nS step. Full plateau formation occurs in branch A and the resulting steady state voltage bias is temporally aligned with the EPSC amplification occurring in branch B. From a somatic potential near rest to the potentials during the plateau, EPSCs are amplified approximately threefold. *Panel B inset*: A pair of EPSCs from the pre- and post-onset regions of the simulation (thick and stippled traces, respectively). The high frequency reservation of the synaptic input can also be seen in the narrowness of the stippled trace. *Panels C and D*: The I-V and F-I functions for the "split-dendrite" model appropriately display hysteresis about zero input. Although the plateau onset (-52.7 mV, 3.38 nA) and offset (-65.5 mV, -3.67 nA) values are within the range observed experimentally, the magnitude of I-V hysteresis is a bit large (ΔV = 12.8 mV); the current magnitude of I-V hysteresis (ΔI = 7.05 nA) is also within the range reported in Table 1.

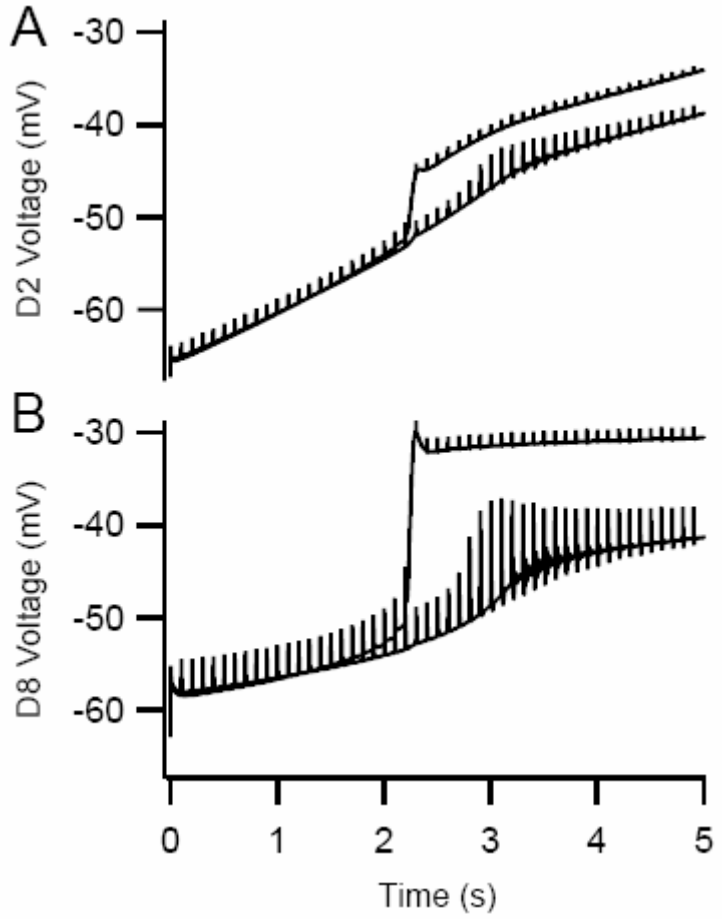

Figure 3.8 *Branchwise differences in dendritic functionality*. Local voltage trajectories during the same synaptic input protocol as in Figures 3.6 and 3.7B. *Panels A and B*: Paired compartments remain isopotential prior to Ca^{2+}-plateau formation. Branch A, containing both Ca^{2+}-plateau and electrotonic compression mechanisms, depolarizes to a steady-state potential between 12 mV (D8) and 5 mV (D2) higher than the corresponding compartments in branch B. *Panel A*: Voltage in the D2 dendritic compartments immediately distal to the branch point (i.e. D2A and D2B). *Panel B*: Voltage profile in the most distal dendritic compartments (D8A and D8B). Note the higher degree of electrical decoupling between these dendritic regions.

Figure 3.8 also shows that the amplification factor measured at the soma is a good indicator of local amplification factors. Individual EPSPs are locally amplified approximately two-fold in the compartments of branch B (i.e. Ca^{2+}-plateau-free branch of the split-dendrite model).

EMERGENT BEHAVIORS

Active Synaptic Integration

In the $Ca_V1.3$[47] model, a curious phenomenon arises in regard to the bi-directional propagation of synaptic input is illustrated in Figure 4.1. The response to a composite input (pulse of 4 nS/compartment conductance change with a superimposed 180 Hz sinusoidal vibration of 1 nS/compartment amplitude for 1 second duration) contains several interesting features. The first is the formation of a dendritic plateau with distal origin which can be seen prior to the first spike at about 50 ms after the onset of stimulation (occurs between 250 and 300 ms in Figure 4.1A). Increases in voltage velocity (which follow the 180 Hz sinusoid) can be seen progressing in the distal to proximal direction over the interval between 305 and 325 ms in Figure 4.1B. Once a sustained, positive rate of rise is achieved in the distal half of the dendritic tree the rate of rise in the initial segment becomes sufficient enough to initiate an action potential. In contrast, during rhythmic firing (Figure 4.1C) this process appears to be occurring in the opposite direction, with a sustained rate of rise initiating proximal to distal prior to the action potential. The tonic spike in Figure 4.1D follows a similar progression where voltage velocity increases originate proximally. The isopotential lines of Figure 4.1B-D are taken directly from Figure 4.1A and the small voltage range in Figure 4.1B demonstrates the electrotonic shortening that occurs during early integration of dynamic synaptic inputs and prior to action potential initiation.

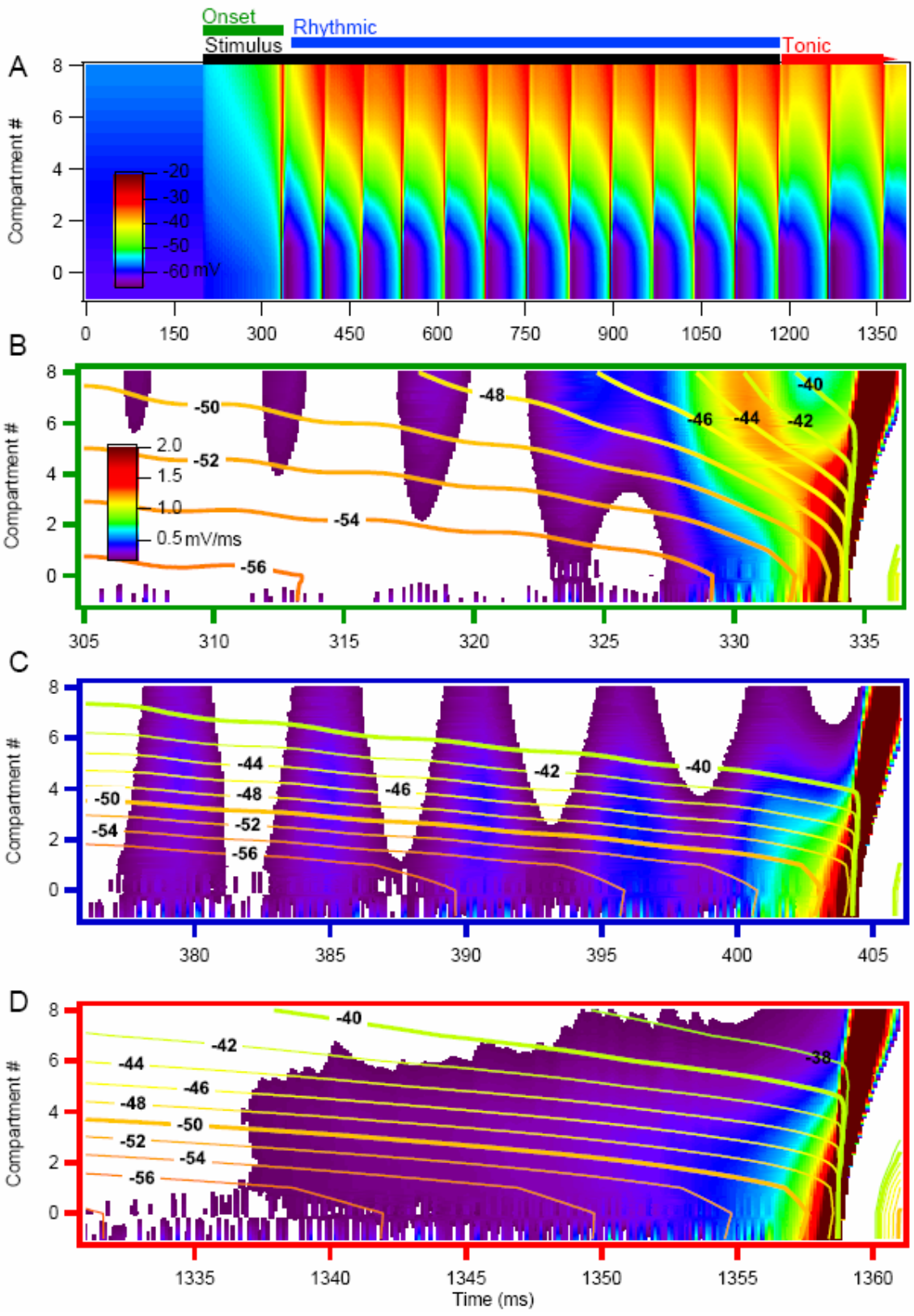
Onset
Rhythmic
Stimulus
Tonic
A
B
C
D
Compartment #
-20
-30
-40
-50
-60 mV
2.0
1.5
1.0
0.5 mV/ms
Time (ms)

Figure 4.1 *Bi-directional propagation of synaptic inputs.* The compartmental voltage profile during a classical TVR protocol (soma = 0, IS = -1). ***Panel A*** illustrates the onset of the dendritic plateau at ~250 ms (approximately 50 ms poststimulus), and the subsequent action potential train arising. Firing does not cease with the withdrawal of synaptic input at t = 200. ***Panel B*** is derived from *A* and indicates a gradual progression, in the distal-to-proximal direction, of action potential initiation. The rate of voltage rise can be seen to progress toward the soma with each vibration and eventually a sustained rate is achieved, between vibrations, in the distal half of the dendritic tree (seen between 325 and 327 ms, just after the rate of rise in the dendrites meets that of the initial segment at the soma). The next vibration yields a marked increase in the dendritic potential trajectory and this increase is maintained in the soma and initial segment. An action potential occurs at about 333 ms, and back-propagates into the dendritic tree. The periodicity of the equipotential lines reflects the 180 Hz excitation until the spike initiation begins to voltage-clamp them. ***Panel C*** displays the subsequent action potential. The subthreshold oscillations follow the 5.55 ms period of the sinusoidal synaptic input and dendritic voltage velocity, again, increases in amplitude and space with each vibration. However, spike initiation proceeds in the reverse direction as panel *B*. ***Panel D*** is the voltage velocity plot of the second tonic spike; initiation again appears to originating from initial segment/soma region. Comparison of the spacing/voltage range of the equipotential lines across panels *B-D* shows the effect of electrotonic compression.

Branchwise Fractionation of the Ca^{2+}-PIC

Plateau formation in the presence of synaptic input exhibits some interesting properties as well. A slow voltage ramp is used to determine the voltage-dependence of this mode of amplification. With the ion channel distributions described above we note some interesting emergent properties of dendritic synaptic integration over differing morphologies.

In Figure 4.2, excitatory input is *uniformly* applied to the branches of a *non-polarized* split-dendrite model version (i.e. mechanisms co-localize everywhere) wherein compartment D1, containing a dense population of SK channels (0.5 μS), is the primary dendritic branch with a pair of 7 compartment daughter branches denoted “A” and “B”. Daughter branches each receive fast, 180 Hz sinusoidal inputs (2 nS/compartment in amplitude) while one branch (branch A in Figure 4.2) receives a mixed-dynamics, excitatory input. This mixed input is simply modeled as a 4 nS/compartment conductance offset to the sinusoid. Panels A through C of Figure 4.2 are snapshots at key time-points of the dendritic fractioning of somatic PIC. About 500 ms after the initiation

of the voltage ramp and synaptic inputs the plateau potential in branch A leads that of branch B by only a few millivolts (Figure 4.2A). One second later the plateau in branch A is fully formed and has begun to impinge on the proximal portion of the nascent plateau in branch B (Figure 4.2B). This impingement remains slight over the next 500 ms due to the current shunt imposed in the proximal compartment (primary branch) by the SK conductance load, and the subsequent plateau formation in branch B proceeds in the distal to proximal direction. After two seconds of elapsed time both daughter branches have fully formed plateau potentials of nearly equal magnitude (Figure 4.2C). The entire time slice of isolated plateau activation in the middle dendritic compartments (D5A/B) is presented in Figure 4.2D.

A rescaled, "dual-split-dendrite" model helped illustrate how the spatial polarization of the dendrites, with regard to functional ion channel distribution, was a corollary of temporal variation in synaptic input dynamics; see Figure 4.3. The distribution of dendritic conductances is as in the "split-dendrite" model with the Ca^{2+}-plateau being allocated to sub-branch 1 in branches A and B (i.e. A1 and B1). An *inhomogeneous* distribution of mixed-frequency, excitatory synaptic input (180 Hz sinusoid of 2 nS + steady-state offset of 4 nS) delivered to all dendritic compartments produced voltage trajectories qualitatively similar to those in Figure 4.2. Synaptic input is distributed such that sub-branch synaptic densities are scaled relative to each other: 4:2:1:3 for A1:A2:B1:B2. With this distribution, dendritic regions for each amplification mechanism (electrotonic compression and Ca^{2+}-plateau) receive the same net input. The first three panels of Figure 4.3 show the branchwise genesis of the plateaus.

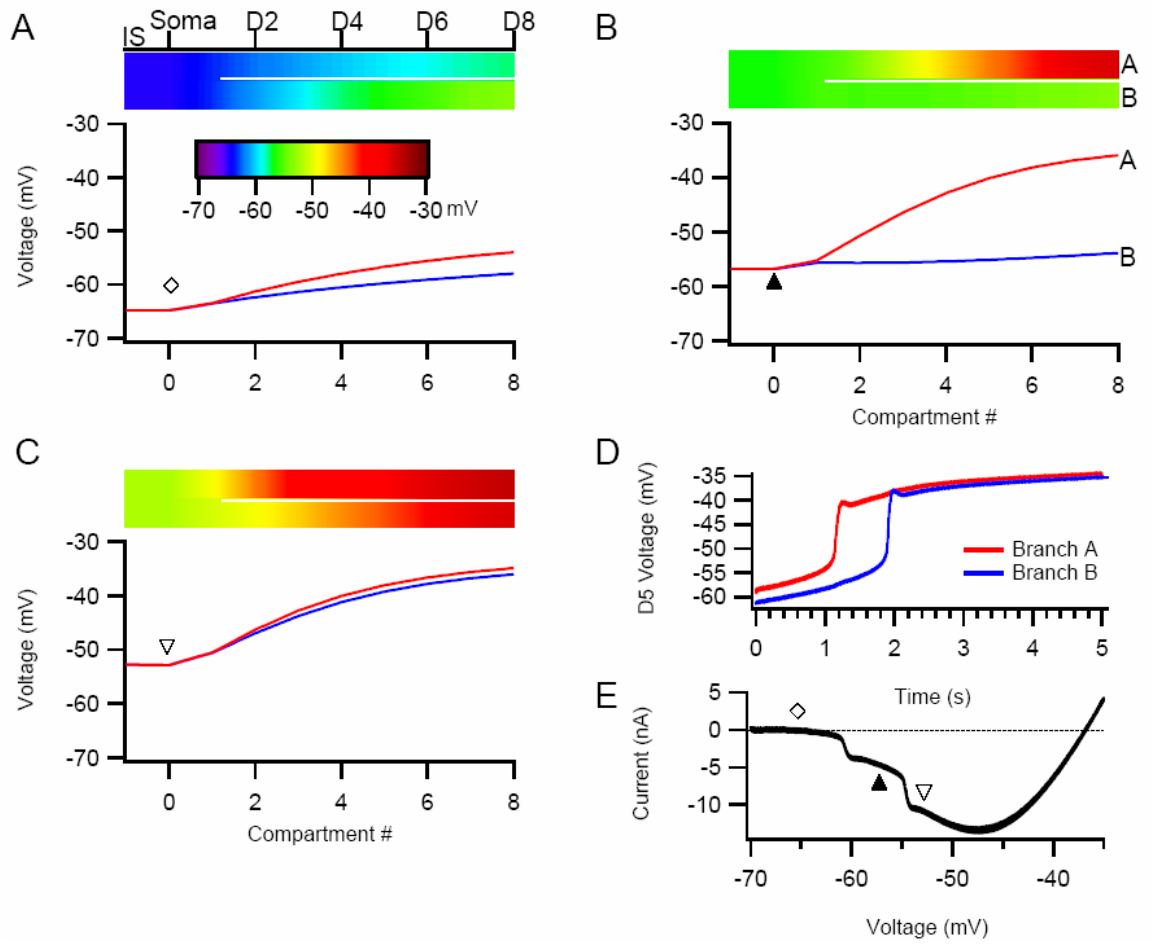

Figure 4.2 *Dendritic fractioning of PICs: uniform synaptic distribution.* Branches A and B each contain seven compartments and share a common primary branch compartment. A ***uniformly distributed***, high-frequency synaptic input is delivered to all dendritic compartments within a particular branch; however branch A receives this input in the presence of an elevated background of excitatory synaptic activity. ***A*:** 625 ms after the beginning of the voltage ramp and synaptic input, the maximal voltage difference between the plateau waveforms is 4 mV. ***B*:** Maximal voltage separation (19 mV) occurs after 1.5 seconds of elapsed time. The color map indicates that most of branch A is depolarized past -40 mV while branch B remains isopotential. ***C*:** After two seconds both plateaus assume a nearly equivalent steady-state where the maximal voltage difference is >1 mV. ***D*:** Voltage trajectory mid-dendrite. ***E*:** Somatic I-V (leak subtracted); symbols in panels *A*,*B*, and *C* denote the somatic potential at a given state of dendritic fractionation, and are mapped to the same points in the somatic I-V function in panel *E*.

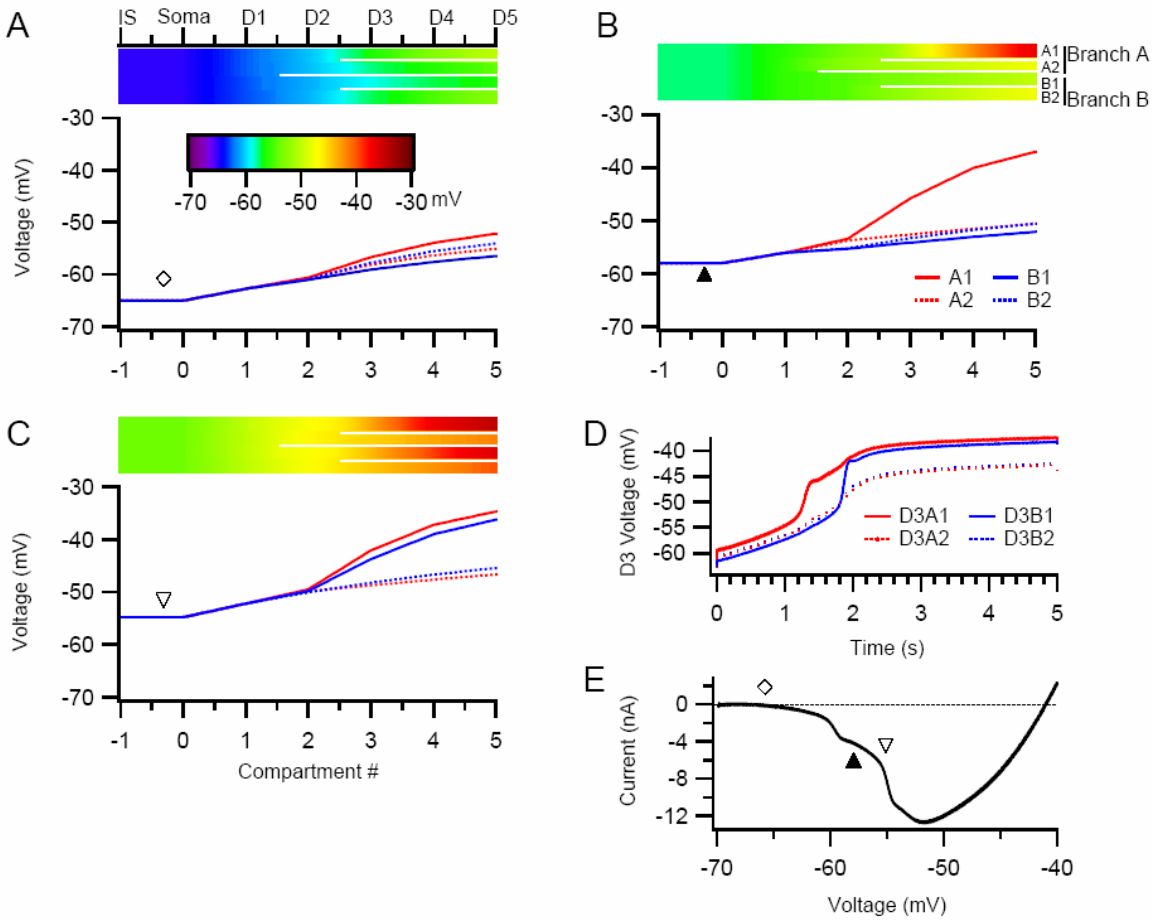

Figure 4.3 *Dendritic fractioning of PICs: inhomogeneous synaptic distribution*. Branches A and B each contain seven compartments and share a common primary branch compartment (D1), while sub-branches 1 and 2 proximally unite at common secondary compartments (D2A and D2B). The dendritic conductance distribution is as in the "split-dendrite" model with the Ca^{2+}-plateau being allocated to sub-branch 1 in branches A and B (i.e. A1 and B1). An ***inhomogeneous distribution*** of high-frequency, excitatory synaptic input is delivered to all dendritic compartments; dendritic regions for each amplification mechanism receive the same net input with sub-branch synaptic weights: 4:2:1:3 for A1:A2:B1:B2. ***A*:** 625 ms after onset of the voltage ramp and synaptic input, the maximal voltage difference between the nascent plateau waveforms is 4 mV. ***B*:** The largest disparity in maximal voltage difference (15 mV) occurs after 1.5 seconds of elapsed time. The color map indicates that most of branch A1 is depolarized past -40 mV while the bulk of the tree remains isopotential. ***C*:** After almost two seconds both Ca^{2+}-plateaus assume a nearly equivalent steady-state where the maximal voltage difference is >1 mV. ***D*:** Per compartment voltage trajectories at mid-dendrite. ***E*:** Leak subtracted somatic I-V; symbols in panels *A*,*B*, and *C* denote the somatic potential at a given state of dendritic fractionation, and are mapped to the same points in the somatic I-V function in panel *E*.

Equivalence of steady-state values of the branchwise-distributed plateaus is a stereotyped occurrence across all dendritic compartments for these synaptic input arrangements. At the soma, a voltage-dependent amplification of synaptic input from spatiotemporally

disparate regions of the dendritic tree occurs in discrete steps. The leak subtracted I-V functions illustrate this in Figures 4.2E and 4.3E with markers corresponding to the somatic potentials at which the PIC has attained a new, transitional value. With *increasing* variety in the background synaptic state of numerous dendritic branches, these transitional values would approximate a continuous (Gaussian) distribution with *decreasing* granularity, thereby smoothly grading the PIC observed at the soma.

DISCUSSION

Over the course of a few decades our view of motoneuron behavior has undergone vast upheaval. The case can be made that rather than passive, integrate-and-fire devices, motoneurons perform much more complex and multi-faceted computations on their inputs. Throughout this expansion of new thought on motoneuron behavior, computer models of motoneurons have lagged behind. This all too common situation has significantly hampered the usefulness of the general-purpose computer to the neuroscience community.

Top-Down vs. Bottom-Up Approaches

Although it has been a fruitful technique, the traditional "bottom-up" approach to constructing conductance-based models of neurons is fraught with issues once the parameter space grows beyond some threshold. Hand tuning is a tractable task with highly reduced models but the inclusion of new, physiological variables invariably increases the dimensionality of the parameter space. Parameter estimation in these larger models has been approached with a variety of methods including automated parameter searches (Vanier and Bower 1999) and genetic algorithms (Taylor and Enoka 2004). However, these techniques are effective only at refining output metrics and fair rather poorly at finding emergent behaviors such as synaptic amplification. A further complication is the likelihood for parameter value non-uniqueness for a given set of model outputs (Bhalla and Bower 1993). The non-uniqueness problem can be mitigated by experimental data. However, in regions less accessible to experimental control, such as the large dendritic tree of mammalian spinal motoneurons, the parameter space is largely unconstrained save for a few rational assumptions.

In contrast, the top-down approach utilized here represents a rational solution for many of the complexity management issues raised above. Additionally, the concept that active conductances are organized to achieve specific goals has a certain teleological appeal and so is not new. For example, it has long been assumed that the ratio of fast sodium currents to potassium delayed rectifier currents was the important factor as opposed to the simply the absolute level of conductance of each (Muller and Lux 1993; Wolff et al. 1998). Additionally, it is common for neuromodulators to directly and indirectly affect several types of ionic conductances simultaneously. For example 5-HT in motoneurons is known to simultaneously reduce TASK (Talley et al. 2000; Perrier et al. 2003), increase L-Type Ca^{2+} (Perrier and Hounsgaard 2003), decrease AHP (Talley et al. 1997), and reduce N-Type Ca^{2+} (Koike et al. 1994; Bayliss et al. 1997).

Another advantage of this type of model specification is that it tends to bring into stark relief the gaps in our understanding of neuronal function. Simply put, if you cannot construct a higher level rule to ensure the specification of a parameter or group of parameters then you do not fully understand their relation to the neuron's function. Thus we can say with confidence that we still do not know how motoneurons function because many parameters remain underspecified. In addition to the issues examined here (i.e. how synaptic amplification relates to bistability), other areas of the motoneuron model remain ambiguous. In particular, the specification of how calcium currents interact with the calcium-dependent SK conductance to form everything from plateau potentials to the AHP is disturbingly open-ended. In this model we, somewhat arbitrarily, linked plateau potentials and the AHP. This worked reasonably well but is admittedly not perfect. Other models have separated the two, solving some of our problems, but introducing problems of their own. We believe that only by a systematic, hypothesis-based exploration of possible mechanisms can we hope to resolve this issue.

Shortcomings of the present methodology

While we have found this type of top-down methodology useful for the specification of motoneuron models, a fundamental prerequisite of such a theory-driven approach is a hypothesis or theory, *apropos*. As such, the present methodology is not amenable to brute-force explorations in any obvious way. Rules must be synthesized from an existing knowledge-base in a manual fashion (i.e. there is, as yet, no automation of "rule-mining") in order to move past the phenomenological realm. In light of the vastness of unknown information processing schemes utilized by single and networked neurons, an automated compilation of elements from a particular knowledge-base into executable (i.e. testable) hypotheses should, indeed, be sought. However, we are not yet at the point where enough is known about the underpinnings of neural function to fully trust the reliability of generalized heuristics necessary to detect and extract pertinent emergent behaviors from experimental and simulated data sets. We excitedly await the development of well-honed statistical inference tools that will make this sort of autoregressive (yet, mechanistically relevant) analysis possible.

Electrotonic Compression vs. Plateau Potentials

This study focused on the mechanisms behind synaptic amplification and bistability in motoneurons. While the widely held belief is that the same L-type Ca^{2+} conductance underlies both of these phenomena we have demonstrated a set of theoretical regulatory mechanisms which effectively divorces the base functions behind these behaviors. The hypothetical mechanism behind synaptic amplification (i.e. electrotonic compression) was ultimately shown to fit well with experimental observations and this study concludes with the strong suggestion that an empirical foundation be laid for such ratiometric arrangements of dendritic conductances conducive to this mechanism.

The additional degree of spatial separation needed to permit the combined action of amplification and plateaus is, itself, an interesting finding. Recent experimental findings (Svirskis et al. 2001) and modeling studies of spinal motoneurons which utilize reconstructed morphologies have suggested that non-uniform distributions of $Ca_V1.3$ may play a functional role in Ca^{2+}-plateau-based amplification (Bui et al. 2006); Bui and colleagues state "…we conclude that the set of L-type Ca^{2+} channels mediating plateau potentials is restricted to discrete regions in the dendritic tree". Our present results support these claims and are furthermore suggestive of the pitfalls encountered when theoretical studies oversimplify the morphological contributions to dendritic computation. Although this might appear to fortify the case for incorporating realistic morphology into motoneuron modeling efforts, our current study has demonstrated how a top-down, or rule-based, methodology can arrive at similar conclusions while both maintaining a model of reduced form and concurrently bounding the vast parameter space of reasonably complex models. What results is nothing short of a scheme which necessarily manages many of the complications confronted by neuronal modelers; this is made possible by ensuring that the intermediate model versions are amenable to intermittent manual (i.e. "hand-tuned") explorations of parameter subspaces. This teleological approach also preserves the simplicity of behavioral abstractions by controlling the degree of complexity added with each incremental expansion advancing toward the highly complex state of realistic morphology.

APPENDIX

CUSTOMARY MATHEMATICAL SPECIFICATION

Simulation

All model outputs were calculated using a custom built simulation environment. Compartmental voltages are computed via numerical integration of initial values and finite differences of state variables.

$$V_m(n+1) = V_m(n) - \frac{\Delta t}{C_m} \cdot \left(\sum_{k}^{Na,K,Ca} I_{j,k} - I_{injected} \right) \Bigg|_{\forall j \in 0...10} \quad (1)$$

where *j* indicates compartment number and *k* denotes each ionic species. Variable step sizes are calculated by a predictor-corrector scheme and values are kept within a logically relevant range (e.g. nonnegative concentrations of mobile charge carriers).

Electrotonic Architecture

The active somatic volume was taken to be 20% of the total volume occupied by a sphere of 60 μm radius; intracellular calcium concentrations were tracked within this space. Radii and lengths of the cylindrical dendrites and initial segment were 25 μm by 6000 μm (combined length of 11 branching levels prior to equivalent cylinder form), and 3 μm by 100 μm, respectively. Specific membrane capacitance, specific membrane resistivity, and axial resistivity were estimated as 1 μF/cm^2, 10300 Ωcm^2, and 70 Ωcm, respectively, in accordance with electrotonic studies of spinal motoneurons by (Clements and Redman 1989).

Detailed description of conductances, pumps and buffers

All transmembrane conductances are based upon a single archetype. Voltage-gating equations follow the general form of:

$$x_\infty = \frac{1}{1 + \exp\left(\frac{(V_m - V_h)}{x_s} \right)} \quad (2)$$

$$\frac{dx}{dt} = \frac{\left(x_\infty - x\right)}{x_\tau} \tag{3}$$

where the particular gating variable is denoted by x, x_∞ is the is the steady-state value of x. V_h is the half-(de)activation voltage, and x_s is a slope term used to indicate the voltage sensitivity of the (de)activation. The rate of change of the gating variable is a function of the gating variable, its steady-state value and time constant (x_τ). In cases in which the time constant is non-constant, but rather a bounded interval or composite function of time and/or voltage, the gating kinetics reflect those characteristics.

The compartments composing the motoneuron model are constructed without specific regard to morphology; instead we target relevant magnitude and scaling of parameters. Therefore, any subsequent reconstructions of the model that aim to take into account the detailed geometries of certain compartments would be advised to target the maximal conductance values (G_{Max}) reported below. In the "split-dendrite" model, compartments distal to the bifurcation still possess the same type and relative ratios for most transporters but the G_{Max} values are half of what is reported below. Exceptions to this are 1) the absence of the persistent calcium conductance in one of the branches and subsequently doubled G_{Max} within the branch to which it is reallocated, 2) the SK G_{Max} is halved in this branch and, 3) the Ca^{2+}ATPase maximal rate is doubled in this branch as well.

Synapses

Dendritically-based, excitatory synapses are modeled as generic Transporter archetypes with a reversal potential of 0 mV (NMDA- or AMPA-like) and a uniform distribution across a given compartment. Therefore, synaptic drive is analogous to a net conductance change of the uniformly distributed proportion of active synapses.

Sodium Channels

The sodium channels incorporated into the model are derived from the Kuo and Bean twelve-state Markov Model. The transition rates between states are adapted from (Kuo and Bean 1994) but in a more simplified form. We reduce the model from twelve states to four states in accordance with the assumption that most of the intermediate transition rates occur at much faster time scales than the final transitions. The twelve-state model is simplified for computational reasons. Practically, this is accomplished by assuming the intermediate activation states are fast and by setting their time constants to zero thereby allowing the steady-state values of their gating variables to be instantaneously reached. The reduced channel model has a pair of half-activation and half-deactivation potentials as well as time constants corresponding to the opened/closed and the deactivation/inactivation state transitions. These parameters for $Na_V1.2$ and $Na_V1.6$ are -32 mV, -45.5 mV, 0.005 ms, 0.2 ms, and -34.5 mV, -47 mV, 0.005 ms, 0.05 ms, respectively. $Na_V1.2$ channels occur solely in the somatic compartment (G_{Max} = 6.0 μS) and are responsible for generating the rapid depolarization underlying the somatic action potential. $Na_V1.6$ channels display a 1.55% non-inactivation, indicating that nearly two percent of a given compartmental population will fail to inactivate and $Na_V1.2$ channels display a 0.8% non-inactivation, together giving rise to a fast sodium PIC. This feature underlies the macroscopic behaviors of rhythmic firing and amplification of rapidly changing inputs. The dendritic distribution of $Na_V1.6$ is homogenous across compartments (G_{Max} = 1.53 μS), with none occurring in the soma, and a second population in the initial segment (G_{Max} = 5.0 μS).

It should be noted that the sodium (de-, in-)activation parameters were derived from a recasting of the Markov kinetics and although their values are rightfully suspect they give rise to the functional behaviors we wished to capture. Parameters such as these are inherently underspecified due to the incongruence of empirical, curve-fitted

representations with analytical functions that do not fully capture the mechanisms that underlie the data. A top-down methodology is one approach to dealing with this under-specification whereby the ill-defined mechanisms may be bounded within a region that defers to hierarchically "higher" behaviors.

Calcium Channels and Calcium Modeling

The voltage-gated calcium channels included in the model are of the HVA L-Type class $Ca_v1.2$ and the L-type $Ca_v1.3$, differing only by their half-activation voltage value. $Ca_v1.2$ is only present in the first dendritic compartment (G_{Max} = 0.86 μS) while the $Ca_v1.3$ ion channel is distributed throughput the dendritic tree (G_{Max} = 0.030 μS). Both channel types have a 1st order voltage-dependent gating, $G_{CaL} = \bar{G} \cdot m$. The half-activation, voltage sensitivity, and time constant for $Ca_v1.2$ and $Ca_v1.3$ are -20 mV, 6 mV, 30 ms, and -41 mV (-47 mV for the $Ca_V1.3^{-47}$ model), 6 mV, 24 ms, respectively.

Sodium-Calcium exchanger (NCX) imports 3 Na^+ with each efflux of Ca^{2+}, thereby producing a net inward current. The rate of exchange, *Flow(ion)*, is simply the instantaneous rate of change:

$$Flow(ion) = \frac{d[ion]}{dt} \tag{4}$$

Accounting for the relative transport ratios, direction, and ion valences the pump current is described by:

$$I = \left(2 \cdot Flow\left(Ca^{2+}\right) - 3 \cdot Flow\left(Na^{+}\right)\right) \cdot F \tag{5}$$

where F is Faraday's constant; 96485 C mol^{-1}.

The pump has a 10 ms time constant simply to control its speed.

$$\frac{dI}{dt} = \frac{I_{\infty} - I}{\tau_{pump}} \tag{6}$$

where the LHS of Equation 6 is capped at 7.25 nA.

Calcium pumps (Ca^{2+}ATPase) are modeled as an outward current proportional to the cytosolic calcium concentration.

$$I = I_{MAX}\left(\frac{\left[Ca^{2+}\right]}{\left[Ca^{2+}\right]+K}\right) \tag{7}$$

where K is the pump half-activation (saturation) and is representative of calcium-sensitivity and the peak electrogenesis (I_{MAX}) is 1 nA in the most proximal compartment and 0.5 nA in the remainder of the dendritic tree (1 nA in D2A-D8A and 0.5 nA in D2B-D8B in the "split-dendrite" model).

The net calcium currents, $Ca_V1.2$, $Ca_V1.3$, Ca^{2+}ATPase, and NCX, are used to determine intracellular calcium concentration:

$$\left[Ca^{2+}\right] = \int\left(\left(z\cdot F\right)^{-1}\cdot I\left(Ca^{2+}\right)_j + Flow\left(Ca^{2+}\right)_j\right)\cdot dt\Big|_{\forall j\in 0\ldots 10} \tag{8}$$

and numerically integrated to update compartmental concentrations:

$$\left[Ca^{2+}\right]_{n+1} = \left[Ca^{2+}\right]_n + \Delta t\cdot\left(\left(z\cdot F\right)^{-1}\cdot I\left(Ca^{2+}\right)_j + Flow\left(Ca^{2+}\right)_j\right)\Big|_{\forall j\in 0\ldots 10} \tag{9}$$

From a reaction perspective, the buffer is simply in a reversible state between free and bound Ca^{2+} ions.

$$Ca^{2+} + B \underset{k_{-1}}{\overset{k_1}{\Leftrightarrow}} B^* \tag{10}$$

where B is the unbound buffer, B^* is the bound buffer and the rate law approximation is:

$$\upsilon_{BAPTA} = k_{-1}\left(\left[B*\right]-\left[B\right]\right) - k_1\left(\left[Ca^{2+}\right]\cdot\left[B\right]\right) \tag{11}$$

The parameters k_1 and k_{-1} are given values to achieve a fast and large buffer; k_{-1} = 5 s^{-1} and k_1 = 20000 $M^{-1}s^{-1}$.

Potassium Channels

All model compartments contain Hodgkin-Huxley type delayed-rectifier potassium channels: (Initial Segment) G_{Max} = 1.0 μS, (Soma) G_{Max} = 4.0 μS and (Dendrites) G_{Max} = 0.905 μS per compartment. The K_{DR} channel kinetics follow the fourth order gating, non-inactivating, HH-like model, $G_{KDR} = \bar{G} \cdot n^4$, as described in motoneurons by Barrett and Crill (Hodgkin and Huxley 1952; Barrett et al. 1980).

$$n_\infty = \frac{1}{1 + \exp\left(\frac{(V_m - V_h)}{n_s}\right)} \tag{12}$$

This channel has a half-activation of -25 mV, voltage sensitivity of 20 mV. The time constant for the K_{DR} conductance is modeled as a voltage-dependent Boltzmann equation with a half- activation of -39 mV and a voltage sensitivity of 5.5 mV, and is subject to the imposed boundary conditions of τ_{Max} = 11.9 ms and τ_{Min} = 1.4 ms.

$$\tau_m = \tau_{Min} + \tau_{Max} \cdot \left(\frac{b}{f}\right) \tag{13}$$

$$b = \exp\left(\frac{V_m - V_h}{b_s}\right) \tag{14}$$

$$f = (1 + b)^2 \tag{15}$$

where *f* and *b* are the forward and backward reaction rates.

SK-type (i.e. K(Ca) or Ca^{2+}-activated potassium) channels occur in two distinct populations. The second through eighth dendritic compartments contain a homogenous distribution, G_{Max} = 0.2 μS (0.05 μS in branch "A" and 0.1 μS in branch "B" of the

"split-dendrite" model), while the most proximal dendritic compartment contains a more substantial load of this particular conductance, G_{Max} = 1.0 μS.

$$I_{K(Ca)} = G_{Max} \cdot m \cdot \left(V_m - E_K\right) \tag{16}$$

$$m(n+1) = m_\infty - \left(m_\infty - m(n)\right) \cdot \exp\left(\frac{-\Delta t}{\tau_m}\right) \tag{17}$$

The SK ion channel exhibits 1st order gating. The 2nd order calcium-dependent steady state value of the gate is given by:

$$m_\infty = \frac{m_d \cdot \left[Ca^{2+}\right]^2}{1 + m_d \cdot \left[Ca^{2+}\right]^2} \tag{18}$$

with a time constant (in ms):

$$\tau_m = \frac{1}{m_b} \cdot \frac{1}{1 + m_d \cdot \left[Ca^{2+}\right]^2} \tag{19}$$

m_b and m_d are 15e3 s^{-1} and 1e5 M^{-2}, respectively.

Miscellaneous Transporters

Na^+/K^+ Leak is specified by a physiologically relevant parameter value on a per compartment basis; we estimated this to be 0.04525 μS.

We fit data from hypoglossal motoneurons (Bayliss et al. 1994) to approximate the h-current time constants. The voltage sensitive activation and deactivation time constants were obtained by single exponential and quadratic fits, respectively:

$$\tau_{act} = 2.07 * \exp\left(\frac{v}{0.04}\right) \tag{20}$$

$$\tau_{deact} = B + \sqrt{B^2 + 0.02}\,;\ B = -\left(7 \cdot v + 0.46\right) \tag{21}$$

where voltage and time are in units of volts and seconds. I_h is non-inactivating, time- and voltage-dependent, with a reversal potential at -38.8 mV, half-activation at -75.0 mV, and a slope factor = 5.3 mV. The activation and deactivation time constants are equivalent (277 ms) at -80.4 mV. This transporter occurs in each dendritic compartment with a G_{Max} = 0.2 μS.

REFERENCES

Barrett EF, Barrett JN, and Crill WE. Voltage-sensitive outward currents in cat motoneurones. *Journal of Physiology* 304: 251-276, 1980.

Barrett JN BE, Dribin LB. Calcium-dependent slow potassium conductance in rat skeletal myotubes. *Dev Biol* Mar;82: 258-266, 1981.

Bayliss DA, Li YW, and Talley EM. Effects of serotonin on caudal raphe neurons: inhibition of N- and P/Q-type calcium channels and the afterhyperpolarization. *J Neurophysiol* 77: 1362-1374, 1997.

Bayliss DA, Viana F, Bellingham MC, and Berger AJ. Characteristics and postnatal development of a hyperpolarization-activated inward current in rat hypoglossal motoneurons in vitro. *Journal of Neurophysiology* 71: 119-128, 1994.

Bennett DJ, Hultborn H, Fedirchuk B, and Gorassini M. Synaptic activation of plateaus in hindlimb motoneurons of decerebrate cats. *J Neurophysiol* 80: 2023-2037, 1998.

Bhalla US, and Bower JM. Exploring parameter space in detailed single neuron models: simulations of the mitral and granule cells of the olfactory bulb. *J Neurophysiol* 69: 1948-1965, 1993.

Booth V, Rinzel J, and Kiehn O. Compartmental Model of Vertebrate Motoneurons for Ca2+-Dependent Spiking and Plateau Potentials Under Pharmacological Treatment. *J Neurophysiol* 78: 3371-3385, 1997.

Bui TV, Ter-Mikaelian M, Bedrossian D, and Rose PK. Computational estimation of the distribution of L-type Ca(2+) channels in motoneurons based on variable threshold of activation of persistent inward currents. *J Neurophysiol* 95: 225-241, 2006.

Carlin KP, Jones KE, Jiang Z, Jordan LM, and Brownstone RM. Dendritic L-type calcium currents in mouse spinal motoneurons: implications for bistability. *Eur J Neurosci* 12: 1635-1646., 2000a.

Carlin KP, Jones KE, Jiang Z, Jordan LM, and Brownstone RM. Dendritic L-type calcium currents in mouse spinal motoneurons: implications for bistability. *Eur J Neurosci* 12: 1635-1646, 2000b.

Clements JD, and Redman SJ. Cable properties of cat spinal motoneurones measured by combining voltage clamp, current clamp and intracellular staining. *J Physiol* 409: 63-87, 1989.

Cook EP, and Johnston D. Active dendrites reduce location-dependent variability of synaptic input trains. *J Neurophysiol* 78: 2116-2128, 1997.

Cook EP, and Johnston D. Voltage-dependent properties of dendrites that eliminate location-dependent variability of synaptic input. *J Neurophysiol* 81: 535-543, 1999.

Cullheim S, Fleshman JW, Glenn LL, and Burke RE. Membrane area and dendritic structure in type-identified triceps surae alpha motoneurons. *J Comp Neurol* 255: 68-81, 1987a.

Cullheim S, Fleshman JW, Glenn LL, and Burke RE. Three-dimensional architecture of dendritic trees in type-identified alpha-motoneurons. *J Comp Neurol* 255: 82-96, 1987b.

Donselaar Y, Kernell D, and Eerbeek O. Soma size and oxidative enzyme activity in normal and chronically stimulated motoneurones of the cat's spinal cord. *Brain Res* 385: 22-29, 1986.

Elbasiouny SM, Bennett DJ, and Mushahwar VK. Simulation of Ca2+ persistent inward currents in spinal motoneurones: mode of activation and integration of synaptic inputs. *J Physiol* 570: 355-374, 2006.

Elbasiouny SM, Bennett DJ, and Mushahwar VK. Simulation of dendritic CaV1.3 channels in cat lumbar motoneurons: spatial distribution. *J Neurophysiol* 94: 3961-3974, 2005.

Fleshman JW, Segev I, and Burke RB. Electrotonic architecture of type-identified alpha-motoneurons in the cat spinal cord. *J Neurophysiol* 60: 60-85, 1988.

Graas EL, Brown EA, and Lee RH. An FPGA-based approach to high-speed simulation of conductance-based neuron models. *Neuroinformatics* 2: 417-436, 2004.

Gustafsson B, and Pinter MJ. Factors determining the variation of the afterhyperpolarization duration in cat lumbar alpha-motoneurones. *Brain Research* 326: 392-395, 1985.

Harvey PJ, Li Y, Li X, and Bennett DJ. Persistent sodium currents and repetitive firing in motoneurons of the sacrocaudal spinal cord of adult rats. *J Neurophysiol* 2005.

Heckman CJ, Lee RH, and Brownstone RM. Hyperexcitable dendrites in motoneurons and their neuromodulatory control during motor behavior. *Trends Neurosci* 26: 688-695, 2003.

Hille B. *Ion Channels of Excitable Membranes*. Sunderland, Mass.: Sinauer Associates, 1992, p. xiii, 607 p.

Hodgkin AL, and Huxley AF. A quantitative description of membrane current and its application to conduction and excitation in nerve. *J Physiol* 117: 500-544, 1952.

Holmes WR, and Rall W. Estimating the electrotonic structure of neurons with compartmental models. *J Neurophysiol* 68: 1438-1452, 1992.

Holmes WR, Segev I, and Rall W. Interpretation of time constant and electrotonic length estimates in multicylinder or branched neuronal structures. *J Neurophysiol* 68: 1401-1420, 1992.

Hounsgaard J, and Kiehn O. Ca++ dependent bistability induced by serotonin in spinal motoneurons. *Exp Brain Res* 57: 422-425, 1985.

Hounsgaard J, and Kiehn O. Serotonin-induced bistability of turtle motoneurones caused by a nifedipine-sensitive calcium plateau potential. *Journal of Physiology* 414: 265-282, 1989.

Hultborn H, Denton ME, Wienecke J, and Nielsen JB. Variable amplification of synaptic input to cat spinal motoneurones by dendritic persistent inward current. *J Physiol* 552: 945-952, 2003.

Keren N, Peled N, and Korngreen A. Constraining compartmental models using multiple voltage recordings and genetic algorithms. *J Neurophysiol* 94: 3730-3742, 2005.

Kernell D. The adaptation and the relation between discharge frequency and current strength of cat lumbrosacral motoneurones stimulated by long-lasting injected currents. *Acta Physiologica Scandinavica* 65: 65-73, 1965a.

Koike H, Saito H, and Matsuki N. 5-HT1A receptor-mediated inhibition of N-type calcium current in acutely isolated ventromedial hypothalamic neuronal cells. *Neurosci Res* 19: 161-166, 1994.

Kuo CC, and Bean BP. Na+ channels must deactivate to recover from inactivation. *Neuron* 12: 819-829, 1994.

Kuo JJ, Siddique T, Fu R, and Heckman CJ. Increased persistent Na(+) current and its effect on excitability in motoneurones cultured from mutant SOD1 mice. *J Physiol* 563: 843-854, 2005.

Larkum ME, Rioult MG, and Luscher HR. Propagation of action potentials in the dendrites of neurons from rat spinal cord slice cultures. *J Neurophysiol* 75: 154-170, 1996.

Lee RH, and Heckman CJ. Adjustable amplification of synaptic input in the dendrites of spinal motoneurons in vivo. *J Neurosci* 20: 6734-6740, 2000.

Lee RH, and Heckman CJ. Bistability in spinal motoneurons in vivo: systematic variations in persistent inward currents. *J Neurophysiol* 80: 583-593, 1998a.

Lee RH, and Heckman CJ. Bistability in spinal motoneurons in vivo: systematic variations in rhythmic firing patterns. *J Neurophysiol* 80: 572-582, 1998b.

Lee RH, and Heckman CJ. Essential Role of a Fast Persistent Inward Current in Action Potential Initiation and Control of Rhythmic Firing. *J Neurophysiol* 85: 472-475., 2001.

Lee RH, Kuo JJ, Jiang MC, and Heckman CJ. Influence of active dendritic currents on input-output processing in spinal motoneurons in vivo. *J Neurophysiol* 89: 27-39, 2003.

Li Y, and Bennett DJ. Persistent sodium and calcium currents cause plateau potentials in motoneurons of chronic spinal rats. *J Neurophysiol* 90: 857-869, 2003.

Li Y, Gorassini MA, and Bennett DJ. Role of persistent sodium and calcium currents in motoneuron firing and spasticity in chronic spinal rats. *J Neurophysiol* 91: 767-783, 2004.

Muller W, and Lux HD. Analysis of voltage-dependent membrane currents in spatially extended neurons from point-clamp data. *Journal of Neurophysiology* 69: 241-247, 1993.

Perrier JF, Alaburda A, and Hounsgaard J. 5-HT1A receptors increase excitability of spinal motoneurons by inhibiting a TASK-1-like K+ current in the adult turtle. *J Physiol* 548: 485-492, 2003.

Perrier JF, and Hounsgaard J. 5-HT2 receptors promote plateau potentials in turtle spinal motoneurons by facilitating an L-type calcium current. *J Neurophysiol* 89: 954-959, 2003.

Powers RK. A variable-threshold motoneuron model that incorporates time- and voltage-dependent potassium and calcium conductances. *Journal of Neurophysiology* 70: 246-262, 1993.

Powers RK, and Binder MD. Effective synaptic current and motoneuron firing rate modulation. *J Neurophysiol* 74: 793-801, 1995.

Prather JF, Powers RK, and Cope TC. Amplification and linear summation of synaptic effects on motoneuron firing rate. *J Neurophysiol* 85: 43-53, 2001.

Richter DW, Schlue WR, Mauritz KH, and Nacimiento AC. Comparison of membrane properties of the cell body and the initial part of the axon of phasic motoneurones in the spinal cord of the cat. *Exp Brain Res* 20: 193-206, 1974.

Safronov BV, Wolff M, and Vogel W. Functional distribution of three types of Na+ channel on soma and processes of dorsal horn neurones of rat spinal cord. *J Physiol (Lond)* 503: 371-385, 1997.

Sah P. Kinetic properties of a slow apamin-insensitive Ca(2+)-activated K+ current in guinea pig vagal neurons. *Journal of Neurophysiology* 69: 361-366, 1993.

Schwindt PC, and Crill WE. Properties of a persistent inward current in normal and TEA-injected motoneurons. *Journal of Neurophysiology* 43: 1700-1724, 1980.

Svirskis G, Gutman A, and Hounsgaard J. Electrotonic structure of motoneurons in the spinal cord of the turtle: inferences for the mechanisms of bistability. *J Neurophysiol* 85: 391-398., 2001.

Talley EM, Lei Q, Sirois JE, and Bayliss DA. TASK-1, a two-pore domain K+ channel, is modulated by multiple neurotransmitters in motoneurons. *Neuron* 25: 399-410, 2000.

Talley EM, Sadr NN, and Bayliss DA. Postnatal development of serotonergic innervation, 5-HT1A receptor expression, and 5-HT responses in rat motoneurons. *J Neurosci* 17: 4473-4485, 1997.

Taylor AM, and Enoka RM. Optimization of input patterns and neuronal properties to evoke motor neuron synchronization. *J Comput Neurosci* 16: 139-157, 2004.

Vanier MC, and Bower JM. A comparative survey of automated parameter-search methods for compartmental neural models. *J Comput Neurosci* 7: 149-171, 1999.

Weinstein RK, and Lee RH. Architectures for high-performance FPGA implementations of neural models. *J Neural Eng* 3: 21-34, 2006.

Wolff M, Vogel W, and Safronov BV. Uneven distribution of K+ channels in soma, axon and dendrites of rat spinal neurones: functional role of the soma in generation of action potentials. *J Physiol (Lond)* 509: 767-776, 1998.

Zengel JE, Reid SA, Sypert GW, and Munson JB. Membrane electrical properties and prediction of motor-unit type of medial gastrocnemius motoneurons in the cat. *Journal of Neurophysiology* 53: 1323-1344, 1985.